

X-ray temperature spectroscopy of simulated cooling clusters

Riccardo Valdarnini¹

SISSA – International School for Advanced Studies, Via Beirut 2/4, Trieste, Italy

Corresponding author : R. Valdarnini

Abstract

Results from a large sample of hydrodynamical/N-body simulations of galaxy clusters in a Λ CDM cosmology are used to simulate cluster X-ray observations. The physical modeling of the gas includes radiative cooling, star formation, energy feedback and metal enrichment that follow from supernova explosions. Mock cluster samples are constructed grouping simulation data according to a number of constraints which would be satisfied by a data set of X-ray measurements of cluster temperatures as expected from *Chandra* observations. The X-ray spectra from simulated clusters are fitted into different energy bands using the XSPEC *mekal* model. The biasing of spectral temperatures with respect to mass-weighted temperatures is found to be influenced by two independent processes. The first scale dependency is absent in adiabatic runs and is due to cooling, whose efficiency to transform cold gas into stars is higher for cool clusters and this in turn implies a strong dependency of the spectral versus mass-weighted temperature relation on the cluster mass. The second dependency is due to photon emission because of cool gas which is accreted during merging events and biases the spectral fits. These events have been quantified according to the power ratio method and a robust correlation is found to exist between the spectral bias and the amount of cluster substructure.

The shape of the simulated temperature profiles is not universal and it is steeper at the cluster center for cool clusters than for the massive ones. This follows owing to the scale dependency introduced by cooling which implies for cool clusters higher central temperatures, in scaled units, than for massive clusters. The profiles are in good agreement with data in the radial range between $\sim 0.1r_{vir}$ and $\sim 0.4r_{vir}$; at small radii ($r \lesssim 0.1r_{vir}$) the cooling runs fail to reproduce the shape of the observed profiles. The fit is improved if one considers a hierarchical merging scenario in which cluster cores can accrete cooler gas through merging with cluster subclumps, though the shape of the temperature profiles is modified in a significant way only in the regime where the mass of the substructure is a large fraction of the cluster mass.

Key words: Methods : numerical – X-ray: clusters – Cosmology : simulations

PACS: 98.65.Cw; 98.65.Hb; 02.60.Cb

1 Introduction

Observations show that most of the baryons present in a galaxy cluster are in the form of a hot ionized gas (intracluster medium, ICM), with temperatures in the range $\sim 10^6 - 10^7 \text{ K}$ (Sarazin 1986). The continuum emission is dominated by bremsstrahlung processes, and is free from the contamination effects which may arise in the optical band. For this reason, observations of galaxy clusters in the X-ray band have been extensively carried out over the past decade (Henry et al. 1992, Ebeling et al. 1997, Rosati et al. 1998). X-ray observations of the spatial distribution of cluster density and temperature allow one to determine, under the assumption of hydrostatic equilibrium, the mass in baryons as well as the dark matter profile and the total cluster mass M_X . The latter quantity is connected to the global cluster temperature T_X , and through the $M_X - T_X$ relation the cluster mass function can then be used to find the cluster X-ray temperature or luminosity functions. Observations of these quantities are thus used to constrain theoretical models (Henry & Arnoud 1991, Edge et al. 1990, Henry 1997, Rosati et al. 1998, Ebeling et al. 1998). Knowledge of the temperature profile is also important in order to assess the role of non-gravitational heating processes which can contribute to the budget of the gas thermal energy. This is relevant because observations show that the cluster scaling relations do not obey the self-similar behavior predicted by gravitational collapse (David et al. 1993, Allen & Fabian 1998, Markevitch 1998). Heating of the ICM by non-gravitational processes will break self-similarity and help to explain the observed relations (Evrard & Henry 1991, Kaiser 1991, White 1991, Loewenstein & Mushotzky 1996, Valageas & Silk 1999, Loewenstein 2001).

A powerful tool for studying the dependence of cluster observational quantities upon theoretical models is given by the use of hydro/N-body simulations. Hydrodynamic simulations have been widely used to investigate the formation and evolution of galaxy clusters (Katz & White 1993, Sugimoto & Ostriker 1998, Anninos & Norman 1996, Yoshikawa, Jing & Suto 2000, Pearce et al. 2000, Lewis et al. 2000, Bialek, Evrard & Mohr 2001, Muanwong et al. 2002, Loken et al. 2002, Valdarnini 2003, Tornatore et al. 2003, Ascasibar et al. 2003), see also Voit (2005) and references cited therein. The advantage over analytical methods is that they can treat the gas evolution self-consistently. The validity of the numerical approach is supported by X-ray observations of surface brightness maps, which indicate the existence of merging substructure (Mohr et al. 1995). Moreover, high resolution observations performed with *Chandra* and XMM-Newton satellites have revealed the existence of complex cluster temperature structure, like shocks induced by mergers and 'cold front' (Markevitch et al. 2000, Vikhlinin et al. 2001, Markevitch et al. 2002).

¹ E-mail: valda@sissa.it

Hydrodynamic simulations in which modeling of the gas physical processes incorporates radiative cooling, star formation and energy feedback from supernovae yield a cluster luminosity-temperature relation in good agreement with data for cluster temperatures $T_X \gtrsim 1keV$ (Valdarnini 2003, Borgani et al. 2004). These results support the radiative cooling model (Bryan 2000), where cluster X-ray properties are determined by the cooling efficiency to turn cold gas into stars. However, there are a number of issues for which hydrodynamic simulations that include the physical modeling of the gas described above do not produce a satisfactory agreement with data. For instance, the radial temperature profiles are not isothermal and decline with radius. At small distances from the cluster center the simulated profiles have a steep rise moving inwards. This behavior is not seen in a set of observations (Markevitch et al. 1998, Allen, Schmidt & Fabian 2001a, De Grandi & Molendi 2002, Vikhlinin et al. 2005, Piffaretti et al. 2005). The data agree with the simulation results at $r \gtrsim 20\%r_{vir}$ but indicate a temperature profile which is flat or declining at very small distances. These data are also at variance with the predictions of the standard cooling flow model (Fabian 1994). In the very central cluster regions the amount of cool gas is smaller than that predicted by the model, with gas temperatures never below $\simeq 1keV$ (Kaastra et al. 2001, Tamura et al. 2001, Peterson et al. 2001). This failure to reproduce temperature data has prompted many authors to consider possible heating mechanisms to explain the lack of cool gas in the cluster core. Among the proposed models, thermal conduction (Voigt et al. 2002, Jubelgas, Springel & Dolag 2004, Dolag et al. 2004, Sijacki & Springel 2006) and energy feedback from active galactic nuclei (Churazov et al. 2001, Brüggen & Kaiser 2001, Böhringer et al. 2002, Fabian et al. 2002, Brüggen & Kaiser 2002, Omma et al. 2004, Reynolds et al. 2005) are the most considered.

The observed temperature profiles are then sensitive to different physical phenomena and can be used to constrain theoretical models. Moreover, as already outlined, the intracluster gas exhibits a complex thermal structure. It is then important to perform properly the comparison of X-ray observations with the results of numerical simulations, taking into account the effects of instrumental response and background contaminations on the spectral fit temperatures. As an additional effect which can bias comparisons, the spectral temperatures are measured in a specified energy bands, whereas the simulated cluster temperatures are theoretically defined according to a specified weighting scheme. This problem has been already analyzed by Mathiesen & Evrard (2001) and, more recently, by Gardini et al. (2004), Mazzotta et al. (2004), Rasia et al. 2005 and Vikhlinin (2006). The aim of this paper is to investigate for systematic effects which can bias spectroscopic measurements of cluster X-ray temperatures. For this purpose, a large numerical sample of simulated clusters is used to construct spatially resolved X-ray spectra as expected from observations with the *Chandra* satellite. The cluster spectral fit temperatures are found using the XSPEC library, and are compared against mean gas temperatures

with theoretically defined averages. Moreover, spatially resolved X-ray spectra of the simulated clusters are also used to investigate how the measured temperature profiles differ from the projected profiles obtained directly from simulations. The comparisons are performed on a statistical basis, using the cluster numerical sample. The numerical sample is also subdivided according to the amount of substructure present in a given cluster, this allows us to investigate how spectral measurements are affected by the cluster dynamical state.

This paper can be considered a generalization of that of Mathiesen & Evrard (2001, hereafter ME), the main differences being the size of the numerical cluster sample used, together with a more complete physical modeling of the gas in the simulations and the X-ray spectroscopic analysis of radial temperature profiles. The paper is organized as follows. The simulations are presented in Section 2, in Section 3 the procedures with which average and spectroscopic temperatures are extracted from the simulated clusters are discussed. Section 4 is dedicated to the method used to measure substructure in the simulated cluster. The results are discussed in Section 5 and the conclusions are drawn in Section 6.

2 Simulations

The simulations were run using a TREESPH code. A detailed description of the simulation procedure is given in Valdarnini (2003, hereafter V03) The cosmological model assumes a flat CDM universe, with matter density parameter $\Omega_m = 0.3$, $\Omega_\Lambda = 0.7$, $\Omega_b = 0.019h^{-2}$ and $h = 0.7$ is the value of the Hubble constant in units of $100Kms^{-1}Mpc^{-1}$. The primeval spectral index of the power spectrum n is set to 1 and the power spectrum has been normalized to $\sigma_8 = 0.9$ on a $8h^{-1}Mpc$ scale. Initial conditions for the cluster simulations are constructed as follows, following a two-step procedure. A collisionless cosmological simulation is first run in a box of comoving size L , using a P3M code with N_p particles, starting from an initial redshift $z_i = 10$.

Clusters of galaxies were located at $z = 0$ using a friends-of-friends (FoF) algorithm, so as to detect overdensities in excess of $\simeq 200\Omega_m^{-0.6}$ within a radius r_{vir} . The corresponding mass M_{vir} contained within this radius is defined as $M_{vir} = (4\pi/3)\Omega_m\rho_c\Delta_c r_{vir}^3$, where $\Delta_c = 187\Omega_m^{-0.55}$ for a flat cosmology and ρ_c is the critical density. A cluster numerical sample is constructed with the cluster identified using this procedure, with the clusters being sorted according to the values of their M_{vir} at $z = 0$. The final numerical sample used in the hydrodynamic simulations consists of two distinct samples, S1 and S2. The first sample comprises the most massive $n_1 = 120$ clusters identified at $z = 0$ in a cosmological run with $L_1 = 200h^{-1}Mpc$ and $N_{1p} = 84^3$ particles. Sample

S2 consists of the n_2 most massive clusters identified in a new cosmological run with box size $L_2 = 400h^{-1}Mpc$ and $N_{2p} = 168^3$. The number $n_2 (= 32)$ of clusters in sample S2 is chosen so that the mass M_{vir} of the n_2 -th least massive cluster is just above that of the first cluster of the sample S1. For sample S2 M_{vir} ranges from $\simeq 10^{15}h^{-1}M_\odot$ down to $2.3 \cdot 10^{14}h^{-1}M_\odot$, while for sample S1 the n_1 -th cluster has $M_{vir} = 10^{13}h^{-1}M_\odot$. The random realization of the initial density perturbations are different in the two cosmological simulations. The final numerical cluster sample of 153 clusters represents then a complete sample of the clusters present in a cubic region of size $400h^{-1}Mpc$ down to virial masses $\simeq 2.3 \cdot 10^{14}h^{-1}M_\odot$, and is undersampled by a factor 8 below this mass and $M_{vir} \simeq 10^{13}h^{-1}M_\odot$.

Hydrodynamic simulations are performed in physical coordinates for each of the clusters present in the sample. The initial conditions are constructed as follows. All of the cluster particles at $z = 0$ which are within a sphere of radius r_{vir} located at the cluster center are identified. These particles are traced back to a redshift $z_{in} = 49$ and a cube of size $L_c \simeq 25 - 50Mpc$ enclosing these particles is placed at the cluster center. A lattice of $N_L = 51^3$ grid points is set inside the cube, and to each node is associated a gas particle with its mass and position. A similar lattice is set for dark matter particles, with the node positions being displaced by one-half of the grid spacing with respect the nodes of the gas lattice. The particle positions are then perturbed, using the same random realization as for the cosmological simulations. High-frequency modes are added to the original random realization in order to sample the increased Nyquist frequency. The gas and dark matter particles used for the hydrodynamic simulations are those for which the perturbed particle positions lie within a sphere of radius $L_c/2$ from the cluster center. To model external gravitational fields these particles are surrounded out to a radius L_c by a spherical shell of low-resolution dark matter particles, each having a mass 8 times the sum of the masses of a gas and dark matter particle of the inner region.

The simulations are evolved to the present using a multistep TREESPH code with a tolerance parameter $\theta = 1$, quadrupole corrections enabled, and minimum timesteps of $\Delta t_{min} = 6.9 \cdot 10^5 yr$ and $\Delta t = 8\Delta t_{min}$ for gas and dark matter particles, respectively. For the clusters of sample S2(S1), simulations have been performed setting $\varepsilon_g = 25(15)kpc$, where ε_g is the gravitational softening parameter of the gas particles. The gravitational softening parameters of other species of particles have been set according to the scaling $\varepsilon_i \propto m_i^{1/3}$, where m_i is the mass of the particle i . The runs have a number of gas particles $N_g \simeq 70,000$, with similar values for the number of dark matter particles in the inner and outer shell. The mass of the gas particles ranges from $m_g \simeq 5.5 \cdot 10^9 M_\odot$ for the first cluster of sample S2, down to $m_g \simeq 6 \cdot 10^8 M_\odot$ for the least massive cluster of sample S1. For the runs considered here this mass resolution can be considered adequate (Valdarnini 2002), yielding final

gas distributions with converging profiles for the simulated clusters. This issue will be discussed in more detail in sect. 6.

Numerical integrations have been performed with comoving softenings out to $z = 20$, after which they are kept fixed in physical coordinates. Hydrodynamic simulations are followed according to the SPH method (Hernquist & Katz 1989), with a minimum smoothing length of $\varepsilon_g/4$. During its evolution the thermal energy equation is subject to energy sinks from recombination and collisional excitation, bremsstrahlung and inverse Compton cooling. The cooling function $\Lambda_c(T, Z)$ depends on the gas temperature and metallicity. Lock-up tables have been constructed from Sutherland & Dopita (1993) and stored in a file. During the simulations, the tabulated values are interpolated to obtain $\Lambda_c(T, Z)$ for the gas particles. Cold gas in high density regions is thermally unstable and is subject to star formation (SF). A gas particle which is in a collapsing region and whose cooling time is smaller than the dynamical time τ_d is eligible to form in a timestep Δt a star particle with half of its mass, at a rate given by the τ_d^{-1} . At each timestep a star particle heats its gas neighbors by supernova (SN) explosions of type II and Ia. The number of SN explosions in the time interval is calculated according to the star particle age and the initial mass function, with each SN explosion adding $\simeq 10^{51}$ ergs to the gas thermal energy. An Arimoto & Yoshii (1987) initial mass function has been assumed (V03), in the mass range from 0.1 to $40M_\odot$. The gas is also metal enriched at each timestep through SN explosions. The mass in metals ejected by a star particle is distributed among its neighbors according to the SPH smoothing procedure. The gas metallicity thus increases with time, and the dependence of the cooling rate on the gas metallicity is taken into account properly. In order to construct simulated X-ray spectra from a given cluster all the relevant hydrodynamical variables of an individual run are output during the simulation at various redshifts, with the smaller ones being $z = 0.025, 0.039, 0.052$.

3 Temperature definitions

In this section the way in which mean cluster gas temperatures and temperature profiles with theoretically defined averages are obtained from simulations data, together with the spectral temperatures, is described. The simulation temperatures are defined as those obtained from theoretically defined averages applied to the gas particle temperatures of output data. A spectroscopic X-ray measurement of a galaxy cluster temperature is constructed with a much less simple procedure. Using output data produced with the runs described in Section 2, X-ray spectra are first obtained from a certain cluster at a specified redshift. As a second step a background component has been added to the spectra, and the resulting spectra have been then properly convolved with a

template area response file (ARF) and redistribution matrix file (RMF) of the *Chandra* observatory. Finally, the generated event files are fitted by a single temperature *mekal* model available with the XSPEC library.

3.1 Simulation temperatures

In the continuum limit an average gas temperature is defined as

$$T_W^R = \frac{\int_0^R T(\vec{x}) W d^3x}{\int_0^R W d^3x}, \quad (1)$$

where W is a weight function and the integral has a spherical boundary of radius R . Common choices for W are the gas density $\rho_g(\vec{x})$ (mass-weighted temperatures, $W = \rho_g$) and the X-ray emissivity $\varepsilon^{(X)}(\vec{x}) = \Lambda^{(X)}(T, Z)n_e n_H$ (emission-weighted temperatures, $W = \varepsilon^{(X)}$), n_e and n_H being the electron and hydrogen gas number density, respectively. The cooling function $\Lambda^{(X)}(T, Z)$ is calculated using a Raymond-Smith (1977) code. Because of the Lagrangian nature of SPH simulations, volume integrals are replaced by a summation over the particles, so that

$$T_w^R = \frac{\sum_i W_i \frac{m_i}{\rho_i} T_i}{\sum_i W_i \frac{m_i}{\rho_i}}, \quad (2)$$

where the subscript i denotes the value of the quantity at the position of the particle i , $\rho = \rho_g$, $w = m$ or $w = ew$ according to the chosen weighting scheme and the summation is understood to be over all the gas particles within a distance R from the cluster center. The cluster center is defined to be the position \vec{x}_c where the gas density reaches its maximum. The position \vec{x}_c is found according to the following iterative procedure: at each iteration $k = 1, 2, \dots, M$ the center of mass is found, $\vec{x}_c^{(k)}$, based on the gas particles which are within a sphere of radius $R^{(k)} < R^{(k-1)}$, located at $\vec{x}_c^{(k-1)}$. The last iteration M is such that there must be at least a number N_M of gas particles within $R^{(M)}$. Robust results are obtained for $N_M \simeq 50 - 100$ and $R^{(k)} = (3/4)R^{(k-1)}$. The cluster center is then defined as $\vec{x}_c^{(M)}$.

The emission-weighted temperature T_{ew}^R is defined using the bolometric emissivity, in a similar way a band-limited emission-weighted temperature $T_{ew}^R(E_1 - E_2)$ can be defined in the energy range $E_1 - E_2$ by using the band-limited emissivity $\varepsilon = \int_{E_1}^{E_2} \varepsilon_\nu d\nu$, where ε_ν is the specific emissivity. It is useful to define a radius R_Δ such that the average density within that radius is Δ times the critical density, i.e. $M_\Delta = 4\pi R_\Delta^3 \Delta \rho_c(z)/3$, where $\rho_c(z) = 3H(z)^2/8\pi G$, $H(z)^2 = H_0^2 E(z)^2$ and $E(z)^2 = \Omega_m(1+z)^3 + \Omega_\Lambda$. Hereafter, average global cluster tem-

peratures will be denoted by T_w^Δ , where Δ takes the values commonly used in literature, i.e. $\Delta = 2500, 500$ and 200 .

Temperature profiles are obtained by first choosing a line of sight and then locating in the plane orthogonal to the line of sight annuli of increasing radii around the cluster center. Hydrodynamic variables are estimated at a set of grid points using the SPH smoothing procedure. The geometry of the grid is cylindrical with coordinates $(\tilde{\rho}, \tilde{\phi}, \tilde{z})$ and the origin is located at the cluster center, the \tilde{z} -axis is along the line of sight. The points are uniformly spaced, linearly in the angular coordinate, and logarithmically in the radial and \tilde{z} coordinates. The range of the spatial coordinates is between $2 \cdot 10^{-4}$ and unity in units of R_{200} . There are $N_{\tilde{\rho}} = 60, N_{\tilde{\phi}} = 20, 2N_{\tilde{z}} = 50$ points in the coordinate intervals. For a continuous distribution the annulus having a finite width with projected radial boundaries b_1 and b_2 has a projected emission-weighted temperature $T(b)$ given by

$$T(b) = \int_{b_1}^{b_2} \tilde{\rho} d\tilde{\rho} \int_{-\infty}^{+\infty} \varepsilon^{(X)} T(\vec{x}) d\tilde{z} \bigg/ \int_{b_1}^{b_2} \tilde{\rho} d\tilde{\rho} \int_{-\infty}^{+\infty} \varepsilon^{(X)} d\tilde{z}, \quad (3)$$

where $b = (b_1 + b_2)/2$ and $|\vec{x}|^2 = \tilde{\rho}^2 + \tilde{z}^2$. The integrals (3) are approximated by first evaluating the corresponding hydro variables at the grid points and then performing the discrete volume integrals over the set of points which are within the given boundaries, the integral along the \tilde{z} -axis is truncated at $|\tilde{z}| = R_{200}$. The projected emission-weighted temperatures are calculated at a set of 20 projected radii, with approximately uniform intervals in $\log b$ and ranging between $b_{min} \simeq 5 \cdot 10^{-3}$ and $b_{max} \simeq 0.5$ in units of R_{200} .

3.2 Spectral temperatures

The simulated spectroscopic temperatures are obtained by fitting the cluster spectral emission with single temperature models. The procedure to obtain spectroscopic temperatures from simulated source spectra consists of three separate steps which are described in what follows. The first step is to obtain photon spectra from a simulated cluster observed at a redshift z along a given line of sight. The photon flux per unit energy S_ν (photons/sec cm^2 keV) that reaches the observer is given by

$$S_\nu = (1+z)^2 L_{\nu(1+z)} / 4\pi d_L^2(z), \quad (4)$$

where d_L is the luminosity distance and L_ν is the volume integral of the specific X-ray emissivity of the cluster: $L_\nu = \int \varepsilon_\nu^{(X)} dV$. The cluster global spectral fit temperatures T_s^Δ , to be compared with the averaged cluster temperature T_w^Δ ,

is obtained from a flux S_ν^Δ with volume integral performed as in Eq. (2), over the same spherical boundaries. The cluster spectral temperature profile $T_s(b)$ is found using for each ring the photon flux $S_\nu(b)$. The fluxes are calculated with the volume integrals over $\varepsilon_\nu^{(X)}$ in Eq. (4) being performed in an analogous way to those over $\varepsilon^{(X)}$ in Eq. (3), using the same grid geometry and boundaries.

The second step consists of manipulating the simulated photon spectra S_ν according to a certain procedure, in order to reproduce the spectroscopic temperatures that would be obtained by fitting the cluster spectra as measured by the *Chandra* Advanced Camera for Imaging and Spectroscopy (ACIS) instrument. In particular, the spectral analysis described here will consider observations relative to the S3 chip of the ACIS configuration. The S3 chip has a small field of view ($\theta_{S3} = 8.4 \text{ arcmin}$), but with a high spatial (1 pixel = 0.5 arcsec) and energy resolution ($\Delta E \simeq 100 \text{ eV}$). For the considered energy band the simulated spectra are then binned into energy channels with width $\Delta E = 100 \text{ eV}$, an energy resolution which is adequate to correctly model the *Chandra* ACIS energy resolution (ME). The cluster global spectral fit temperatures T_s^Δ are calculated in two energy bands: $[2 - 10]$ and $[0.5 - 10] \text{ keV}$. Spectroscopic temperature profiles $T_s(b)$ are instead considered in the energy band $[0.5 - 7] \text{ keV}$. Hereafter it is understood that all the considered energy bands are corrected for the cluster redshifts. Once the fluxes S_ν have been discretized the files which contain the spectral distribution $S_{\Delta E}$ are transformed into new files $S_{\Delta E}(XS)$, written in the FITS file format². This format allows the files to be read by the XSPEC (v 11.3.0) library³ used to construct the modeled spectra.

The background is modeled by adding a background file $B_{\Delta E}(XS)$ to each spectral file $S_{\Delta E}(XS)$. The file $B_{\Delta E}(XS)$ with the proper spectral distribution of background photons is constructed as follows. The normalization parameters are first calculated using, for different energy bands, the quiescent background rates B_a (photons/sec arcmin²) taken from Tables 1 and 2 of Markevitch⁴. For a mock observation with exposure time t_{exp} , aperture angle $\Delta\theta$ and a given energy band, the corresponding background rate is used to calculate the expected number of background photons N_B .

A file $B_{\Delta E}(XS)$ with a background spectrum is then created from a template background file⁵ using the *fakeit* command in XSPEC. The spectrum is convolved with the appropriate ARFs and RMFs used to mimic the instrument responses (see Sect. 3.4), which are the same pair of matrices used to perform the convolution of the source spectrum $S_{\Delta E}(XS)$. The parameters of the background file are rescaled so that when integrating the spectrum over

² <http://fits.gsfc.nasa.gov/>

³ <http://heasarc.gsfc.nasa.gov/docs/xanadu/xspec/>

⁴ <http://exc.harvard.edu/contrib/maxim/bg/index.html>

⁵ http://exc.harvard.edu/cal/Acis/Cal_prods/bkgrnd/current/

t_{exp} seconds there are N_B photons in the energy band under consideration. To this end the files are manipulated using the utility *fparkey* from the FTOOLS library ⁶. A companion file $B_{\Delta E}^{(mk)}(XS)$ is created for later use with the same procedure. At this stage the binned source spectrum $S_{\Delta E}(XS)$ is convolved with the ARF and RMF files of the mock observation using the *atable* tool, available with XSPEC. The produced pulse height amplitude (PHA) file and the corresponding background file are added together by applying to the files the *mathpha* utility of the FTOOLS library. Errors in each energy bin are calculated using the Poissonian statistic. The resulting spectrum is then grouped using the task *grppha* of the same library, so that the energy channels contain at least 20 photon counts.

Spectral analysis is then finally performed in the third step. The spectrum is analyzed with XSPEC, provided that a certain number of constraints are satisfied. These constraints take into account the instrumental limits of the receiver and are described later (see Sect. 3.3). If the spectrum does not violate any of these constraints then the fit is performed modeling the emission with a single-temperature optically thin plasma. This emission model is the single-temperature *mekal* model implemented with XSPEC and has three free parameters: the gas temperature, the metallicity abundance and the normalization; the other parameters being kept fixed. The spectrum is background subtracted using the background file $B_{\Delta E}^{(mk)}$ previously generated. Errors at the 68% confidence level (c.l.) for the considered parameters are estimated using the tasks *error* and *steppar*.

3.3 Construction of spectral temperature data sets

The construction of spectral samples is constrained by the instrumental limits of the receiver. For the considered emission models and energy bands the spectral fit procedure described here is applied to a simulated cluster at redshift z if a number of constraints are satisfied. These constraints are chosen so that a mock sample of spectral temperatures is generated which satisfies a number of properties as those of a set of spectral temperatures obtained from real cluster data. These constraints are set as follows. The signal-to-noise ratio (S/N) is calculated as

$$S/N = \sqrt{t_{exp}P}/\sqrt{P+B}, \quad (5)$$

where P is the source photon rate (photons/sec), $B = B_a\pi(\Delta\theta)^2$ is the photon background rate, $\Delta\theta$ the source angular aperture and t_{exp} is the observation time. For global cluster temperatures the spectral samples are constructed

⁶ <http://heasarc.gsfc.nasa.gov/lheasoft/ftools/>

using data from the simulation ensemble at redshifts $z = 0.087, 0.47, 0.85$. For a given energy band the exposure time is held fixed for all the clusters at all the redshifts, $t_{exp} = 220ks$ for the energy interval $[0.5 - 10]keV$ and $t_{exp} = 440ks$ for the interval $[2 - 10]keV$. In order for the spectral fits to be performed, a first criterion that must be satisfied is that the number of source photons must exceed a minimum threshold of $N_\gamma > 250$. Another criterion is that the cluster spectra must have a signal-to-noise ratio of at least $S/N > 10$. This threshold selects spectra of good quality, and at high redshifts this prevents the spectral fitting of background dominated spectra.

Spectral fits are performed in the energy band $[2 - 10]keV$ only for those cluster with $T_{mw}^{200} > 2keV$. Spectral temperature profiles are constructed from simulation data at redshifts $z = 0.116, 0.052, 0.039$ and $z = 0.025$. For these spectra $t_{exp} = 140ks$ for all the clusters and redshifts in the considered energy band $[0.5-7]keV$. The spectrum of each annulus is fitted if it satisfies $N_\gamma > 250$ and $B < 2P$. The last criterion extracts from the ring under consideration spectra having S/N with high values ($\simeq 10^2$). This removes from the spectral sample fits of poor quality, though a large number of spectra can still be fitted. For global cluster temperatures the redshifts have been chosen in order to highlight the biases associated with the cluster selection owing to the detector physical limits. Therefore there are three different and well separated redshifts rather than the redshift distribution which would be expected from a real cluster catalog. For spectral temperature profiles the adopted range of redshifts was motivated by the need to mimic that of the clusters for which temperature profiles are measured (see, for example, Vikhlinin et al. 2005).

The following constraints take into account the finite field of view of the S3 chip. For global cluster temperatures spectral analysis is performed only if $\theta_\Delta \equiv R_\Delta/d_A(z) < \theta_{S3}/2 = 4.2'$, here $d_A(z)$ is the angular distance in a flat cosmology. For the spectral temperature profiles a ring spectrum is fitted only if the ring has inner radius $r_{in}/d_A(z) > 4''$ or outer radius $r_{out}/d_A(z) < 4'$, and thickness $(r_{out} - r_{in})/d_A(z) > 5''$. Finally, a spectral fit temperature is rejected if, for the considered number of degrees of freedom (d.o.f.), the statistic of the fitted model gives a value of the χ^2 larger than the threshold value χ_c^2 for which the null hypothesis probability is larger than 10 %. Values of χ_c^2 were pre-calculated as a function of the number of d.o.f. up to $d.o.f. = 1,000$ and stored in a table which was used at run time. The range of values for the reduced $\chi_\nu^2 \equiv \chi^2/d.o.f.$ of the fits lies between 0.5 and unity, with the bulk of the values clustered around 0.5.

3.4 Construction of the Response Functions

The instrumental response of the ACIS-S3 detector is position dependent, but can be considered approximately constant within each of the 32x32 square regions covering the chip. For extended sources, weighted ARFs and RMFs are then constructed by summing the corresponding subregion matrices, with a weight proportional to the photon count of the spectral image in the region under consideration (Gardini et al. 2004). Here a simplified treatment is adopted, in which the source emission is first integrated spatially, and then the single source spectrum is convolved with appropriate template ARFs and RMFs. For an isothermal gas the two methods give the same results, if there is a temperature gradient then photons far from the cluster center will be in proportion weighted more than in the procedure which sums over subregions. Therefore, this implies on average global cluster temperatures biased toward lower values, with respect the first method. Because the bulk of the emission is concentrated at the cluster center, this effect is however expected to be negligible. The same arguments apply to the photon spectra extracted from cluster annuli, for which it is assumed that spatial variations of the gas temperature within a single annulus can be neglected.

If one considers a large number of spectra, the weighting errors associated with a single convolution can be statistically reduced if the source spectra are convolved with weighted ARFs and RMFs extracted from a template observation of a cluster with a regular gas distribution. This cluster must have the characteristic of being in a highly relaxed state and of covering a large field of view in the ACIS-S3 chip. To this end Abell 2029 was chosen, for which analysis of the ACIS-S3 image (Lewis, Stocke & Buote 2002) shows a very regular structure and a spatial extent $\simeq 4'$ wide. The cluster is located at $z = 0.0767$, spectral analysis yields an intracluster gas temperature $T_X \simeq 8keV$ and a virial radius $r_{vir} \simeq 2.5Mpc$. The cluster exhibits a regular X-ray morphology and there is no evidence of a cooling flow at the cluster center. A set of weighted ARFs and RMFs was generated with different geometrical boundaries using the tool *acisspec* of the CIAO ⁷ version 3.0.2, with calibration database CALDB (version 2.28). The selected source regions are centered on the peak of the X-ray emission, with their geometry being chosen to approximately fit that of the analyzed spectra. For each source spectrum, the pair of response matrices with geometrical boundaries providing the best fit to those of the considered source is chosen in order to be convolved with the binned source spectrum $S_{\Delta E}(XS)$. The same pair is later used when the spectrum is fitted using the single-temperature emission model *mekal* implemented with XSPEC. The main advantage of the procedure described here is that the adopted approximation allows one to analyze with a reasonable

⁷ <http://exc.harvard.edu/ciao>

computational cost a large number of spectra, as it is in this paper.

4 Statistic of cluster substructure

Spectroscopic measurements of the cluster X-ray temperatures can also be affected by the cluster dynamical state (ME). The amount of substructure present in the inner mass distribution of a galaxy cluster is closely related to its dynamical state (Richstone, Loeb & Turner 1992) and many statistical measures have been proposed to quantify cluster substructure (Buote 2002 , and references cited therein). Analysis of X-ray images does not suffer from projection effects which are present in the optical band and the X-ray surface brightness is expected to qualitatively follow the morphology of the projected cluster mass density (Buote 2002). For this reason, in this work is adopted the power ratio method (Buote & Tsai 1995) as a statistical indicator of the cluster dynamical state. The method has been widely used to study cluster X-ray morphologies (cf. Buote 2000). An application of this method to analyze global morphologies of simulated clusters was already performed in an earlier paper (Valdarnini, Ghizzardi & Bonometto 1999), and a systematic statistical analysis of the evolution of cluster X-ray morphology using hydrodynamic simulations in different cosmological models is in preparation (Buote et al. 2006).

The method works as follows. The X-ray surface brightness $\Sigma_X(\rho, \varphi)$ along a given line of sight is the source term of the pseudo potential $\Psi(\rho, \varphi)$ which satisfies the 2-D Poisson equation. The pseudo potential is expanded into plane harmonics and the $m - th$ coefficients of the expansion are given by :

$$\alpha_m = \int_{R' \leq R} d^2x' \Sigma_X(\vec{x}') R'^m \cos(m\varphi'), \quad (6)$$

$$\beta_m = \int_{R' \leq R} d^2x' \Sigma_X(\vec{x}') R'^m \sin(m\varphi'), \quad (7)$$

where $\vec{x}' = (\rho, \varphi)$ and the integration is over a circular aperture of radius R, which is also termed the aperture radius $R \equiv R_{ap}$. The $m - th$ power ratio is then defined as

$$\Pi^{(m)}(R_{ap}) = \log_{10}(P_m/P_0) , \quad (8)$$

where

$$P_m(R_{ap}) = \frac{1}{2m^2}(\alpha_m^2 + \beta_m^2) \quad m > 0, \quad (9)$$

$$P_0 = [\alpha_0 \ln(R_{ap}/\text{kpc})]^2. \quad (10)$$

The ratio P_m/P_0 is a measure of the amount of structure present on the scale of the aperture radius R_{ap} . For a relaxed configuration $\Pi^{(m)} \rightarrow -\infty$. The values of P_m depend on the choice of the coordinate system. If the origin is the center of mass then P_1 vanishes and $\Pi^{(2)}$ is a measure of the degree of flattening (Buote 2002). Large values of P_3/P_0 indicate asymmetric distributions and this ratio will be used in the subsequent analysis as an indicator of the amount of substructure present in a cluster. The moments $P_m(R_{ap})$ of a chosen cluster at a given redshift are calculated along a line of sight as in Eq. 2, by performing the integrals (6),(7) according to the SPH prescription. The origin of coordinates is set at the peak of the X-ray emission.

In order to analyze how spectral fits are affected by the amount of substructure present in a cluster, three separate cluster sub-samples were extracted from the cluster sample. The sub-samples were generated by first constructing the cumulative distribution of the sample values of Π_3 , and then identifying those clusters with a value of Π_3 below the threshold values which define the 25%, 50% and 75% percentile of the cumulative distribution, respectively. Cluster sub-samples will be cross-correlated with values of the spectroscopic temperatures in order to investigate how the cluster dynamical state can bias spectroscopic measurements.

5 Results and discussion

This section is dedicated to analyzing the dependence of spectral fit temperatures, as obtained from simulation data using the procedures described in sect. 3, against cluster temperatures defined according to weighted averages. Global cluster temperatures are discussed in the first two parts, projected temperature profiles from individual clusters are presented in the third part.

5.1 Global cluster temperatures: effects of cooling

The spectral fits temperatures T_s^Δ are obtained by applying the prescriptions of sect. 3 to a cluster sample which is constructed by grouping data from the simulation ensemble at redshifts $z = 0.087, 0.47$ and $z = 0.85$. Those clusters for which the values of Π_3 exceed the threshold value which defines the 50% percentile of the cumulative distribution have been removed from the cluster sample. For those clusters which are part of a cluster sub-sample, identified

by a given value of redshift z and overdensity Δ , the cluster power ratios were calculated according to the procedures described in sect. 4, by choosing the values of the aperture radius R_{ap} to match the radius R_{Δ} (see sect. 5.2). The power ratio cumulative distributions were then constructed for these cluster sub-samples. This procedure has the effect of removing from the cluster sample most of those clusters undergoing a major merger event, thus disentangling the effects of cooling from those due to merging when analyzing the biasing of spectral fit temperatures . The choice of the threshold value is somewhat arbitrary, nonetheless it has been found that the results obtained are fairly robust against changes in the chosen value.

As far as concerns the dependence of the sample on redshift, at high redshifts the construction of the sample is mainly limited by noise, for example the most massive cluster at $z = 0.85$ has $r_{200} \simeq 1.2Mpc$ and in the $[0.5 - 10]keV$ energy band it emits $N_{\gamma} \simeq 4, 200$ photons. The photon count rate of the source is $c/s \simeq 2 \cdot 10^{-2}sec^{-1}$, with a similar value for the background rate. The latter depends on the source size through $B \propto \Delta\theta^2$. At low redshifts the sample construction is limited by the geometrical limits and the main contribution is given by the low temperature clusters. In the $[2 - 10]keV$ bandpass the sample construction is mainly constrained by the photon threshold $N_{\gamma} > 250$, because of the low number of photons emitted by the clusters. In the following analysis mass-weighted temperatures, which are supposed to be fair tracers of the virial values, will be taken as reference temperatures with which to correlate emission-weighted temperatures or spectral temperatures. For a fixed cluster overdensity Δ linear fits of logarithmic variables will be of the form $\log_{10} T_{ew,s}^{\Delta} = a + b \log_{10} T_{mw}^{\Delta}$, with errors on spectral fit temperatures given by the fit of the XSPEC *mekal* model and those on the best fit parameters will be assumed at the 68% c.l..

The correlation between emission-weighted temperatures and spectral temperatures versus mass-weighted temperatures are displayed in Fig. 1 for different overdensities and energy bands. Within a different panel different symbols are for different overdensities Δ , the lines associated with the Δ symbols correspond to the linear fits, with the coefficients a and b given in Table 1. For the sake of clarity random subsamples are plotted. There is a robust correlation between T_{ew}^{Δ} and T_{mw}^{Δ} with $T_{ew}^{2500} \simeq T_{mw}^{2500}$. At smaller overdensities this is not satisfied, with T_{ew}^{200} being systematically higher than T_{mw}^{200} . Emission-weighted temperatures weight preferentially the inner core regions and change a little when going from $\Delta = 2500$ to $\Delta = 200$, whereas T_{mw}^{200} drops to smaller values when R_{Δ} gets higher. From Table 1 $T_{ew}^{200}/T_{mw}^{200} \simeq 1.35(T_{mw}^{200})^{-0.01}$, so that T_{ew}^{200} is $\simeq 30\%$ higher than T_{mw}^{200} , with a weak scale dependence on T_{mw}^{200} . These results are at variance with those of ME. A comparison with their Fig. 5 shows that the relation T_{ew} versus T_{mw} is approximately around the line of equality, with some preference for the scattered points to lie above the line, i.e. $T_{mw} \gtrsim T_{ew}$. These differences must be ascribed to the different physical modeling of the

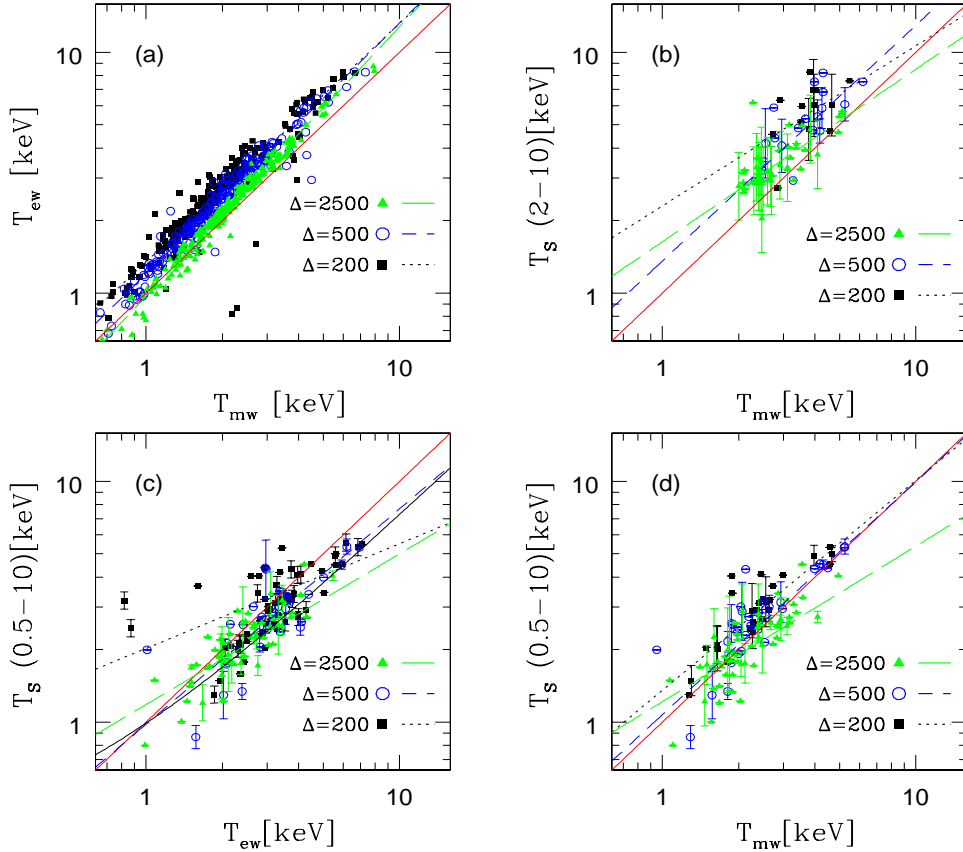


Fig. 1. Spectral temperatures T_s are plotted as a function of the cluster mass-weighted (T_{mw}) or emission-weighted (T_{ew}) temperatures. Upper panel (a) refers to T_{ew} versus T_{mw} . For T_s the numbers in parenthesis indicate the energy band in keV. The temperatures are found according to the procedures described in Sect. 3 and are defined within cluster overdensities $\Delta = 2500$ (filled triangles), $\Delta = 500$ (open circles) and $\Delta = 200$ (filled squares). The diagonal line is the line of equality, the line associated with the Δ symbol corresponds to the linear fit given in Table 1. For the sake of clarity not all of the points and not all of the error bars are shown.

gas in the hydro simulations. In ME the gas was treated adiabatically, here the runs incorporate radiative cooling and star formation, as well as SN feedback. In the cluster central region the gas is subject to radiative losses and cold gas which is Jeans unstable is removed because of star formation. Previous analyses (Lewis et al. 2000, Valdarnini 2002) have shown that taking into account these effects has the consequences of changing the overall temperature profile, with a temperature decline with the radius being steeper than in the adiabatic runs. This is the main reason for the discrepancy found between the behavior of T_{mw} versus Δ here and in ME. It must be stressed that this discussion refers to relative differences between mass and emission-weighted temperatures, when compared against the corresponding ones in the adiabatic

runs.

It is useful to perform a comparison between absolute values. The relation between mass-weighted temperatures of different runs can be calibrated using the mass-temperature relations. For $\Delta = 500$ Eq. (6) of ME gives $M_{500} - T_{mw}^{500}$. The analogous relation here is (for $h=1$)

$$\log_{10} E(z)M_{500} = (13.39 \pm 3 \cdot 10^{-4}) + (1.68 \pm 8 \cdot 10^{-4}) \log_{10} T_{mw}^{500}. \quad (11)$$

To ease the notation in the following discussion the superscript Δ is dropped from the temperatures, the letter c stands for the cooling runs performed here and a refers to the adiabatic runs of ME. By equating the two mass-temperature relations one finds

$$T_{mw}(a) = (0.77 \pm 0.04)T_{mw}(c)^{1.06 \pm 0.02}, \quad (12)$$

this allows us to relate $T_{ew}(a)$ to $T_{mw}(c)$ using the linear fits coefficients of Fig. 6 of ME. This yields

$$T_{ew}(a)/T_{ew}(c) \simeq (0.52 \pm 0.03)T_{mw}(c)^{0.08 \pm 0.02}. \quad (13)$$

So that cooling runs have emission-weighted temperatures which are for $\Delta = 500$ a factor $\simeq 2$ higher than in the corresponding adiabatic runs. Similarly, the ratio for mass-weighted temperatures is

$$T_{mw}(a)/T_{mw}(c) \simeq (0.77 \pm 0.04)T_{mw}(c)^{0.07 \pm 0.01}. \quad (14)$$

Therefore, mass-weighted temperatures are then higher by a factor $\simeq 1.4$. The ratio T_{ew}/T_{mw} is higher than in ME by a factor $\simeq 30\%$, with a weak dependence on T_{mw} . It is found

$$\left[\frac{T_{ew}}{T_{mw}} \right]_{(a)} / \left[\frac{T_{ew}}{T_{mw}} \right]_{(c)} \simeq 0.67 T_{mw}(c)^{0.125 \pm 0.01}. \quad (15)$$

These relations show how incorporating into the simulations a more realistic physical modeling of the gas leads to differences in the gas temperature and distribution which can have a strong impact on temperature averages. This suggests that also the relationships between spectral temperatures and mean gas temperatures can be modified when the simulations take into account the effects of radiative cooling and star formation. The relationships between spectral fit temperatures and averaged gas temperatures are shown in the other panels of Fig. 1.

Table 1

Values of the best-fit coefficients and 1σ confidence limits for linear fits of the form $\log T_w^\Delta = a + b \log T_w^\Delta$ applied to the cluster emission-weighted, mass-weighted and spectral temperatures in keV units. The coefficients are calculated for cluster temperatures defined within radii enclosing cluster overdensities $\Delta = 2500, 500, 200$. The fits are performed over samples which are constructed grouping data from the simulation ensemble at redshifts $z = 0.087, 0.47, 0.85$. The subscript $w = ew, mw, s$ indicates the weighting schemes, described in Sect. 3. For spectral temperatures the numbers in square brackets indicate the energy band. An asterisk in the column of the linear fit coefficient a means that the χ^2 probability of the fit is below 0.01.

$\Delta = 2500$				$\Delta = 500$				$\Delta = 200$				Temperature relations
a	$\sigma_a \cdot 10^2$	b	$\sigma_b \cdot 10^2$	a	$\sigma_a \cdot 10^2$	b	$\sigma_b \cdot 10^2$	a	$\sigma_a \cdot 10^2$	b	$\sigma_b \cdot 10^2$	
-0.013	0.4	1.12	1	0.08	0.5	1.05	1.5	0.13	0.8	0.99	2.3	$T_{ew} - T_{mw}$
0.07	0.8	0.63	2.6	-0.009	3.5	0.9	5.7	0.3(*)	3.5	0.43	6	$T_{s[0.5-10]} - T_{ew}$
0.085(*)	0.8	0.64	2.8	0.03	3	0.97	5.8	0.13	4	0.87	8	$T_{s[0.5-10]} - T_{mw}$
0.21	5.2	0.72	13	0.14	23	0.98	37	0.36	35	0.66	58	$T_{s[2-10]} - T_{mw}$

From Fig. 1(d) it can be seen that in the energy band $[0.5 - 10]$ keV the relationship between T_s and T_{mw} for $\Delta = 2500$ has many points which are approximately distributed according to the linear regression fit, nonetheless the χ^2 probability of the fit is below 0.01. This follows because, as a consequence of selection effects, there are many points of good statistical quality which are at low temperatures. The best-fit parameters are mostly weighted by these points, and the best-fit line follows their distribution. This is more clearly illustrated in Fig. 2, where in the left panel (a) are shown all of the points with which the spectral sample $T_{s[0.5-10]} - T_{mw}$ for $\Delta = 2500$ is constructed. Only spectral temperatures with χ^2 values from the spectral fits below the threshold value χ_c^2 have been plotted. For a given number of d.o.f. χ_c^2 is such that the χ^2 probability of the fit gives $P_{\chi_c^2}(d.o.f.) = 10\%$. As previously outlined at high z 's the construction of the sample is constrained by noise, with only massive clusters being selected, whereas at low redshifts cool clusters are preferentially selected. The poor quality of the linear fit is mainly determined by the relatively large number of outliers which are present at high z 's in the spectral sample and which do not follow the distribution of the low temperature clusters. This feature is closely related to the way in which the introduction of cooling affects the gas distribution.

ME argue that spectroscopic temperatures $T_s[0.5 - 10]$ are biased toward lower values of the mass-weighted temperatures because spectroscopically determined temperatures are weighted by the fitting process according to the photon counts, which are dominated by the low-energy part of the spectrum. From the spectral sample of Fig. 2(a) it can be seen that for massive clusters spectral temperatures are lower than mass-weighted temperatures, whereas $T_s \simeq T_{mw}$ as cool clusters are considered. This behavior follows from two effects: the way in which the sample is constructed and the introduction of the physical modeling of cooling in the simulations. At high redshifts the sample is dominated by massive clusters for which $T_s \lesssim T_{mw}$, as in ME, at low redshifts

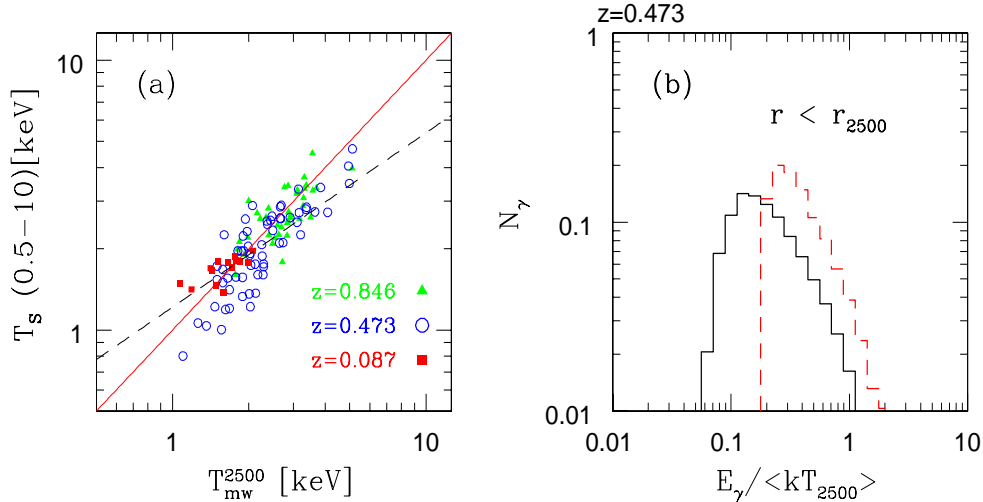


Fig. 2. In panel (a) it is shown for $\Delta = 2500$ the relation between $T_s[0.5 - 10]$ and T_{mw}^{2500} of Fig. 1(d), different symbols refer to clusters selected at different redshifts. The dashed line is the linear fit of Table 1. (b): The source photon distribution emitted within R_{2500} at $z = 0.473$ is binned as a function of the photon energy in units of the average gas temperature. Continuous (dashed) line is the average over the 20 most (least) massive clusters of the sample. Vertical units are arbitrary.

the sample population is dominated by cool clusters. For these clusters, according to the cooling scenario (Bryan 2000, Voit & Bryan 2001), the efficiency of galaxy formation is higher than in hot clusters. This implies a removal of the low-entropy cooled gas, transformed into stars, and a subsequent inflow of the surrounding high-entropy gas. Therefore, in this scenario, it follows that for cool clusters the central cluster temperature, in units of a characteristic cluster temperature, is higher than for massive clusters. This issue will be discussed in more detail in the section dedicated to analyzing the temperature profiles. Fig 2(b) shows the energy distribution of the photons emitted at $z = 0.473$ within R_{2500} by the gas particles of the the 20 most (least) massive clusters of the spectral sample. Energy is in units of the averaged gas temperature within R_{2500} : $\langle T_{2500} \rangle = \sum_i T_i / N$, where the summation is over all of the N gas particles within the radius.

The histograms of the two distributions clearly indicate that cool clusters will have average temperatures higher, when rescaled to a characteristic mean gas cluster temperature, than the corresponding ones of massive clusters. Spectroscopic temperatures too are expected to follow this behavior and, as a consequence, will have a dependence on mass-weighted temperatures different from that found by ME. The argument can be quantified in more detail by applying again the same arguments which lead to Eq. 12. From Fig. 6 of ME

it is found in the $[0.5 - 10]$ bandpass for $\Delta = 500$

$$T_s(a) = (0.6 \pm 0.05)T_{mw}(c)^{(1.1 \pm 0.03)}, \quad (16)$$

and

$$T_s(a)/T_s(c) \simeq (0.56 \pm 0.05)T_{mw}(c)^{(0.13 \pm 0.06)}. \quad (17)$$

Using this equation $T_s(c) \simeq 1.8T_s(a)$ for $T_{mw} = 1\text{keV}$ but $T_s(c) \simeq 1.3T_s(a)$ at $T_{mw} = 10\text{keV}$. This shows that incorporating cooling into the simulations has the net effect of introducing for spectral temperatures a scale dependency much stronger than in the adiabatic runs of ME. The runs performed here take into account the dependence of the cooling function on the gas metallicity; line emission from cold gas is expected to bias significantly spectral temperatures toward lower values (ME), from the results found here it turns out that this bias is largely covered by the scale dependency introduced by cooling. The scale dependency of the $T_s - T_{mw}$ relationship is also dependent on the energy bandpass, as it is found in ME, when passing from the energy interval $[0.5 - 10]\text{keV}$ to $[2 - 10]\text{keV}$ panel (b) of Fig. 1 shows that cool clusters have now $T_s \gtrsim T_{mw}$ at $\Delta = 2500$. This follows because the low energy photons which weight spectral temperatures towards lower values are removed when the spectral fitting is performed in the $[2 - 10]\text{keV}$ range.

These combined effects on the scale dependency of T_s versus T_{mw} are equally present when the cluster radius R_Δ , within which the temperatures are found, is increased. Here the scale dependency is also affected by the biases associated with the cluster selections because of the geometrical constraints that limit the sample construction. Thus, the cluster sample with $\Delta = 200$ of Fig. 1(d) is expected to be less populated by massive clusters than the corresponding sample with $\Delta = 2500$. This is because most of the clusters at $z = 0.087$ have θ_{200} greater than the field of view of the S3 chip. This bias is relatively unimportant in the determination of the slope of the $T_s - T_{mw}$ relationship for $\Delta = 200$, which is dominated by the general tendency of having spectral temperatures higher than mass-weighted temperatures. This behavior was already detected when discussing the relationship between T_{ew} and T_{mw} versus Δ and it is a consequence of incorporating cooling into the simulations. According to the simulation results mass-weighted temperatures have a strong dependency on Δ , whereas T_s or T_{ew} remain relatively unaffected when R_Δ is increased because their weighting scheme favors the central regions where the bulk of the emission is located. Therefore it turns out that spectral temperatures are systematically higher than mass-weighted temperatures when $\Delta \lesssim 10^3$. These results are at variance with those of ME, for which spectral fit temperatures are biased against mass-weighted temperatures by a $\simeq 20\%$ toward lower values.

There is also a well defined tendency to have large statistical errors on the spectral fit temperatures when the overdensity Δ decreases. This effect is present in all of the panels of Fig. 1, where a spectral T_s is correlated with a weighted average gas temperature. The errors σ_a and σ_b on the best fit parameters are given in Table 1 and indicate this tendency. These large errors on the spectral T_s as R_Δ is increased are likely to be induced by the inclusion within the spectral fit volume of an increasing amount of gas at temperatures lower than those at the cluster center. In the $[2 - 10]$ keV bandpass the cluster spectral temperatures with $\Delta = 200$ (Fig. 1(b)) have large statistical errors. The slope of the $T_s - T_{mw}$ relationship is greater than one, but with a statistical error as large as the slope itself. As a general rule it is found that in the energy range $[2 - 10]$ keV, spectral fits temperatures have large statistical errors. This is mainly due to the poor quality of the photon statistics associated with the fits. This is closely related to the construction of the spectral temperature data sets. There is an important difference between the way in which spectral temperature data sets are constructed here and in ME. Each spectrum is fitted by ME, using an isothermal spectral fit model *mekal* with fixed metallicity, keeping the number of observed photons constant to 20,000. At variance with ME, here the exposure time is kept fixed, so that the observed number of photons can vary from cluster to cluster. This choice was motivated by the request of creating spectral temperature sets from fake observations with realistic exposure times, therefore avoiding the selection biases associated with the inclusions in the spectra data set of cluster spectra with an otherwise low photon count. As a consequence, spectral fits in the $[2 - 10]$ keV energy band have generically a poor statistic, because of the smaller number of photons with respect to the $[0.5 - 10]$ keV band, even with the very high exposure time (see sect. 3.3) of 440ks.

In Fig. 1(c) for different overdensities Δ the relationships between $T_s[0.5 - 10]$ and T_{ew} are displayed. These have the same scale dependencies as those between T_s and T_{mw} . The correlations between $T_s[0.5 - 10]$ and T_{ew} can then be explained using the arguments previously discussed. As a general result it appears that T_s - T_{ew} relationships are more widely scattered around the line of equality than their counterparts T_s - T_{mw} . This effect is particularly severe when the overdensity $\Delta = 200$ is considered. This is most likely due to the combined effects of the inclusion within the spectral fit volume of clumps of cold dense gas as R_Δ increases and to the ρ^2 dependence of the T_{ew} measure. There is a tendency for the ratio of T_s to T_{ew} to be higher than that of T_s to T_{mw} , because of the biasing between T_{ew} and T_{mw} . A comparison with previous results can be performed for the relation $T_s[0.5 - 10]$ - T_{ew} at $\Delta = 500$. From a cluster sample obtained from a set of hydrodynamical simulations, with a physical treatment of the gas similar to that used here, Rasia et al. (2005) found a relationship at $\Delta = 500$ between T_{ew} and a suitably averaged temperature T_{sl} . The latter is supposed to be a good approximation to the spectroscopic temperature $T_s[0.5 - 10]$. A linear fit of the form $T_{sl} = aT_{ew} + b$

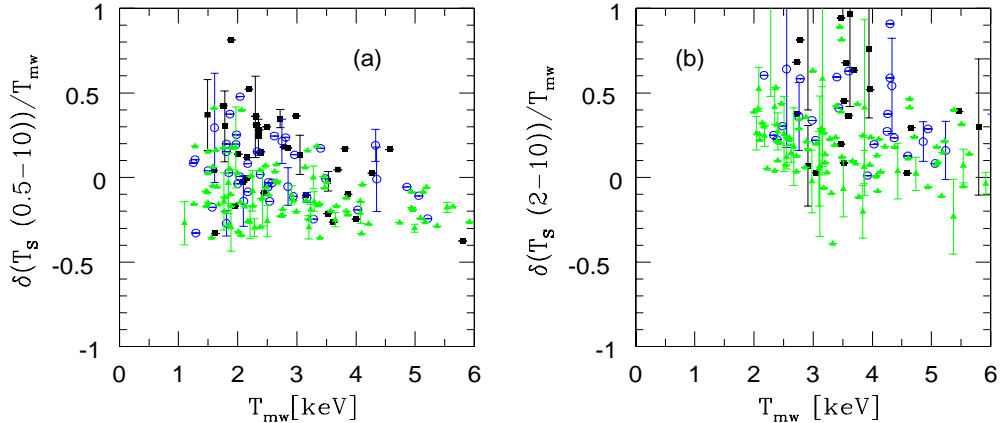


Fig. 3. Relative differences between spectral or emission-weighted temperatures versus mass-weighted temperatures. The temperatures are found as in Fig. 1 and different symbols correspond to different cluster overdensities : $\Delta = 2500$ (filled triangles), $\Delta = 500$ (open circles) and $\Delta = 200$ (filled squares). The notation $\delta(y)/x$ stands for $(y - x)/x$. As in Fig. 1, random subsamples are plotted to avoid overcrowding.

yields $a = 0.7 \pm 0.01$ and $b = 0.29 \pm 0.05$. This relationship is in good agreement with the corresponding one in Table 1. At $T_{ew} = 1 \text{ keV}$ the values of $T_s[0.5-10]$ and T_{sl} are nearly equal, whereas at $T_{ew} = 10 \text{ keV}$ there is a $\sim 10\%$ difference between the two values.

The scale dependencies of the quantities shown in Fig. 1 are more clearly illustrated in Fig. 3, where the fractional differences between correlated quantities are plotted. Panel (a) shows that the quantity $\delta(T_s(0.5 - 10))/T_{mw}$ for $\Delta = 2500$ is characterized by negative values for $T_{mw} \gtrsim 3 \text{ keV}$, and by a plume of positive values as long as $T_{mw} \rightarrow 1 \text{ keV}$. This feature is exacerbated when considering spectral temperatures in the energy band $[2 - 10] \text{ keV}$ (panel (b)), as expected because of the lack of low-energy photons. These results can be compared with Fig. 8 of ME, for which the condition $T_s < T_{mw}$ is always valid in the $[0.5 - 10] \text{ keV}$ bandpass. The behavior of $\delta(T_s(0.5 - 10))/T_{mw}$ for $\Delta = 2500$ is reproduced also when considering temperatures defined within overdensities $\Delta = 500$ or $\Delta = 200$, here the distributions are characterized by a smaller number of massive clusters because of selection constraints. It is clear that the scale dependency of spectral temperatures against mass-weighted temperatures is dominated by the effect of introducing cooling in the simulations. The biasing of spectral temperatures associated with line emission from cool gas was dominant in previous runs which considered only gas shock-heating, but it appears now as a secondary effect.

5.2 Global cluster temperatures: effects of substructure

The discussion of the relationship between spectral and mass averaged temperatures has not yet considered the role of merger events during the individual cluster formation history. According to ME accretion and merger events will alter the measurement of spectral temperatures. These are expected to be significantly biased during a major merger event. As the gas gets shock-heated because of the collision its temperature and luminosity will temporarily increase. The merging will proceed with the subclump of cold gas moving toward the cluster center and with its presence will bias the cluster spectrum toward lower temperatures. The gas of the clump is expected to be cooler than most of the gas in the cluster because of its smaller mass with respect to that of the cluster. ME argue that spectral temperatures will be much smaller than mass-weighted temperatures in the proximity of a merger event.

The substructure statistic used here is the power ratio method described in sect. 4. This statistic is different from the one used by ME and has the main advantage of giving a measurement of the amount of structure present on a given scale, chosen accordingly to the value of the aperture radius R_{ap} . This allows us to correlate, for different overdensities or radii R_{Δ} , the fractional differences $\delta(T_{mw})/T_S$ as a function of the power ratio $\Pi_3 = \log_{10} P_3/P_0$. For the clusters under consideration, the values of R_{ap} have been chosen to match that of the radius R_{Δ} . The two panels of Fig. 4 refer to $\delta(T_{mw})/T_S$ as a function of Π_3 for T_S in the energy bands $[0.5 - 10]$ and $[2 - 10]keV$. In each panel the distributions as obtained by considering the three different overdensities previously considered are displayed. A striking result of Fig. 4(a) is the robust correlation which is found between $\delta(T_{mw})/T_S$ and the substructure as measured by Π_3 . A result which is likely due to the theoretical framework of the statistical method used to measure substructure, which has the advantage of introducing well defined scale dependent quantities. In the $[2 - 10]keV$ band-pass there is a significant correlation only for $\Delta = 2500$ and $\Delta = 500$, the other distribution ($\Delta = 200$) being scattered similarly to the corresponding one of Fig. 3(b).

The correlations are confirmed from the values of Table 2 in which are reported the Spearman rank correlations and significance levels of the corresponding panels. The correlation behavior reveals that T_S is significantly lower than mass-weighted temperatures as Π_3 approaches zero, i.e. whenever the cluster gas distribution is strongly perturbed, which is an indicator of a merging event. As long as Π_3 becomes very large and negative the cluster is in a relaxed state and spectral temperatures T_S are higher than mass-weighted temperatures. For $\Delta = 200$ two clusters have been chosen as representative of these two regimes, they are identified by the circle drawn around their points; their phase-space diagrams are illustrated in Fig. 5.

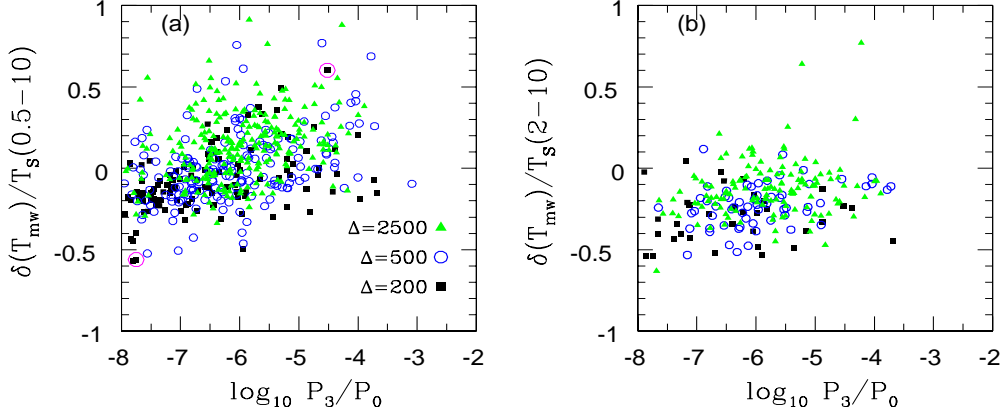


Fig. 4. Relative differences between mass-weighted temperatures and spectral temperatures are shown versus the cluster power ratios $\Pi_3 = \log_{10} P_3/P_0$. The temperatures are defined as in Fig. 1 within different cluster overdensities Δ . The values of Π_3 are calculated at the same redshift and line of sight of the corresponding cluster temperatures. The aperture radii are defined according to the value of Δ , with $R_{ap} = R_{200}$, $R_{ap} = R_{200}/2$ and $R_{ap} = R_{200}/4$ chosen to approximately match the value of R_Δ in correspondence of $\Delta = 200, 500, 2500$, respectively. The two clusters identified by a circle in panel (a) have their phase space diagram plotted in Fig. 5.

The phase-space diagrams of the two clusters in a different dynamical state are displayed in Fig. 5. Gas particle temperatures T_i are in units of T_{mw}^{200} and the solid line gives $T_i = 2keV$. Left panel (a) is for the cluster identified by the circle lying at the bottom left corner of Fig. 4 (a). The cluster is in a fairly relaxed state with $T_{mw}^{200} = 1.8keV$, $\Pi_3 = -7.75$ and will be termed as 'quiescent'. In the right panel (b) the $\log T - \log n$ points for the cluster marked by the circle in the top right part of Fig. 4(a) are plotted. For this cluster $T_{mw}^{200} = 5.8keV$ and $\Pi_3 = -4.52$. The cluster can be considered strongly asymmetric along the chosen line of sight, its value of Π_3 being above the threshold value defining the 75% percentile of the cumulative distribution. This cluster will be denoted as 'active'. The main difference between the two distributions is the long tail of cool gas which characterizes the active cluster, for which $T_s \simeq 0.6T_{mw}^{200}$. Note that the quiescent cluster has most of the material at temperatures below the solid line indicating $2keV$, nonetheless for this cluster $T_s \simeq 2T_{mw}^{200}$.

These findings support the analysis of ME, for whom clusters with an undergoing merging activity have spectral temperatures smaller than mass-weighted temperatures. It must be stressed that the scale dependencies of spectral temperatures which are shown in the panels of Fig. 4 are independent from those function of mass-weighted temperatures which follow by introducing cooling in the simulations. According to these results, the biasing of spectral temperatures can be described in terms of a two-parameter model. A first scale dependency is introduced by cooling and is a function of the cluster mass

Table 2

Spearman linear correlation coefficients r_s and significance levels P_{rs} are given for the fractional temperature differences displayed in the two panels of Fig. 4 as a function of the cluster power ratios Π_3 . Values of P_{rs} below 10^{-2} have been rounded to zero and a significance level of 5% is used to reject the null hypothesis $r_s = 0$.

$\Delta = 2500$		$\Delta = 500$		$\Delta = 200$		fractional temperature - power ratio relations
P_{rs}	r_s	P_{rs}	r_s	P_{rs}	r_s	
0.00	0.31	0.00	0.38	0.00	0.47	$\delta(T_{mw})/T_s[0.5 - 10] - \log_{10}P_3/P_0$
0.01	0.21	0.00	0.39	0.65	0.08	$\delta(T_{mw})/T_s[2 - 10] - \log_{10}P_3/P_0$

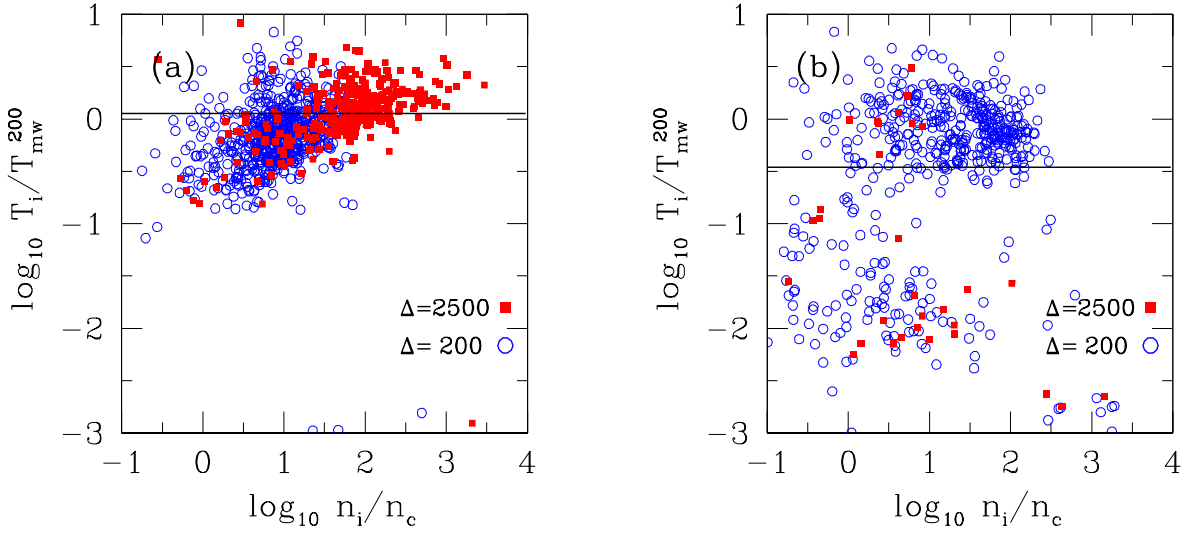


Fig. 5. Phase-space diagrams of the two clusters identified in Fig. 4(a) by the circles drawn around the plotted points. Left panel (a) is for the cluster lying at the bottom left part of the panel. Temperatures are in units of $T_{mw}^{200} = 1.8$ (5.8) keV for the left (right) cluster. The number density ratios are defined as $n_i/n_c = \rho_i/\rho_c(z)$. Filled symbols are for gas particles within R_{2500} and open symbols for those within R_{200} . The continuous line gives $T_i = 2keV$.

or mass-weighted temperature. The second dependency is correlated with the amount of cluster substructure and is independent from the first. Given the importance of this argument it has been decided to look at the phase-space diagram of a cluster with its position in Fig. 4(a) as close as possible to the one identified by the active cluster, but characterized by a low value of T_{mw}^{200} . A cluster was chosen with $T_s \simeq 0.7T_{mw}^{200} (\simeq 1keV)$ and $\Pi_3 = -4.36$. For this cluster, a distribution of points in the $\log T - \log n$ plane very similar to that of the active cluster was found. This confirms that the two processes which govern the biasing of spectral temperatures, subclump accretion and radiative cooling, introduce scale dependencies which can be considered independent of each other.

Finally, there is a further source of biasing which is due to selection constraints because of the detector configuration. At high redshifts the sample construction is limited by noise, whereas at low redshifts the detector geometry is dominant. The relationships between spectral and mass-weighted temperatures are then shaped by these selection effects, which weight the scale dependency introduced by cooling according to the cluster redshift. Spectroscopic measurements with other X-ray telescopes will give relationships different from those obtained here using the *Chandra* ACIS-S3 detector, though qualitatively similar. Because of the limits to the instrument sensitivity the generic population of a cluster sample will be dominated at low redshifts by cool clusters and at high redshifts by massive clusters. Another issue concerns the geometrical limits of the detector, if its field of view is larger than that of the chip S3 spectral relationships for $\Delta = 200$ are expected to include a number of massive clusters larger than the one of Fig. 1 (d). This in turn implies a scale effect which will change the bias between T_S and T_{mw} . This effect is however expected to be negligible since most of the new clusters will be characterized by $T_s \simeq T_{mw}$. Thus the scale dependencies of spectral temperatures found here are expected to be qualitatively reproduced with other detectors.

5.3 Radial temperature profiles

In this section the behavior of the radial temperature profiles as obtained from the sets of simulated spectral samples constructed according to the procedures described in Sect. 3 are discussed. Spectral temperature profiles $T_S(r)$ are compared against projected emission-weighted temperature profiles $T_{ew}(r)$, the spectral fits are performed in the energy band $[0.5 - 7]keV$ and the emission-weighted temperatures are defined in the same energy band. The emission-weighted profiles have been calculated keeping fixed the chosen line of sight and the radial binning, in units of r_{200} , for all of the clusters. For a given cluster, the corresponding spectral temperature profile is obtained by fitting the photon spectra of the considered rings. Because of the scale dependencies previously discussed, the sample of temperature profiles has been subdivided by grouping individual profiles into sub-sample according to several cluster properties. A cluster is part of a subsample denoted by 'hot' if its value of T_{mw}^{200} exceeds $4keV$, 'normal' if $T_{mw}^{200} > 2keV$ or 'cool' when $T_{mw}^{200} < 2keV$. Moreover, the subsamples are also separated according to the degree of regularity of the gas distribution of its cluster members. A cluster is part of a subsample denominated 'quiescent' if the value of Π_3 is below the threshold value which defines the 25% percentile of the cumulative distribution of the power ratios. Similarly, clusters which are members of the 'active' subsample have their value of Π_3 above the threshold which defines the 75% of the percentile of the distribution.

For a given subsample, the mean spectral temperature profile is defined by averaging the profiles of all the clusters of the subsample, with the constraint that a profile is part of the mean if there are at least five spectral temperatures with contiguous radial bins which satisfy the constraints of Sect. 3.3. This criterion was introduced because it has been found that otherwise there would have been clusters with very few annulus bins which would have taken part in the construction of the mean of the profile. These clusters with a very sparse sampling of their profile lead to a distortion of the average profile owing to the scale dependency introduced by cooling. If a cluster spectral profile is accepted to be part of the mean of a given subsample, then the corresponding cluster emission-weighted temperature profile is also part of the average emission-weighted profile for the subsample under consideration. Averages have been performed by rescaling the cluster temperatures to T_{mw}^{200} or $T_{ew}^{200}[0.5 - 10] \equiv T_X$, so that it is the rescaled profile which is averaged. This allows us to compare consistently mean spectral profiles with mean emission-weighted profiles. In order to properly compare with available data profiles, the cluster temperature T_X has been calculated by excluding a central region of size $50h^{-1}kpc$.

The upper panels of Fig. 6 show the projected spectral temperature profiles as a function of r/r_{200} . Within a given panel points with different symbols refer to mean spectral profiles as obtained from different subsamples previously defined; dashed lines are the mean emission-weighted profiles extracted from the same subsample. The profiles of quiescent clusters are displayed in the right panel, those of the active cluster in the left panel. The top right panel of Fig. 6 shows that quiescent clusters have scaled profiles which rise toward the cluster center, reaching their peak values at $r \simeq 0.02r_{200}$ and with a steep decline thereafter. Spectral profiles follow this behavior, but with a biasing which is strongly dependent on the chosen subsample. For hot clusters $T_S(r) \simeq T_{ew}(r)$ whereas for cool clusters this is valid only in the inner regions. Moving outward from the peak value the bias can be as high as $\simeq 20\%$. The discussions of the previous sections suggest that these biasing dependencies can be explained as follows: spectroscopic measurements are biased by line emission toward lower values than emission-weighted temperatures, this effect is negligible for hot clusters but relevant for those clusters of the $T < 2$ subsample. This biasing is strongly suppressed at small radii because of the cooling efficiency for these clusters, which has removed most of the cold gas at the cluster cores. The same arguments apply to the active clusters of the left panel. Here, however, the profiles are shallower than those of the right panel and the peak heights are much more modest. Normal and hot clusters have their profiles approximately isothermal, in the cluster inner regions spectral temperature profiles are now also biased with respect emission-weighted profiles. These dependencies of the shape of the profiles on the value of Π_3 indicate that the effects of merging on the gas distribution of the clusters are the main source for the differences in the profiles. According to this framework active clusters

have profiles much shallower than quiescent clusters because their cores have accreted from subclumps a significant amount of cool gas through a number of merging events. For small values of the aperture radius ($R_{ap} \lesssim r_{200}/4$) the differences between the shape of the profiles from active and quiescent clusters are not as well defined as those displayed in Fig. 6. This suggests that cool gas can significantly accrete into cluster cores only through major merging events, where the mass of the subclump is a significant fraction of the cluster mass.

The solid lines in the upper panels of Fig. 6 indicate the 68% confidence limits of the best-fit profile of Allen, Schimdt & Fabian (2001a). The profile was originally scaled in units of T_{2500} and r_{2500} , here it has been rescaled in units of T_{200} and r_{200} . For the considered sample of clusters $\langle T_{2500} \rangle / \langle T_{200} \rangle \simeq 1.31$ and $\langle r_{200} \rangle / \langle r_{2500} \rangle \simeq 2.78$, with small dispersions. The best-fit profile exhibits a decline in the cluster inner region and an approximate isothermality between $r \simeq 0.1r_{200}$ and $r \simeq 0.3r_{200}$. From Fig. 6 it can be seen that the simulated profiles are unable to follow this behavior. They have a steep rise toward the cluster center, with peak values located at $r \simeq 0.02r_{200}$. Moreover they decline outward with radius, whereas the best-fit profile stays approximately constant. However it must be stressed that the sample of Allen et al. is somewhat peculiar in this aspect. Declining temperature profiles have been recently measured by a number of authors (Vikhlinin et al. 2005, Piffaretti et al. 2005), using spatially resolved spectra obtained from *Chandra* or *XMM-Newton* satellites. The rescaled profiles are quite similar, with a decline in temperature from its peak value at $r \simeq 0.1r_{200}$ toward outer radii. A possible explanation for this discrepancy is suggested by analyzing the differences between the profiles of different subsamples. From the top-right panel of Fig. 6 it can be seen that the average profile of cool clusters is steeper than that of hot clusters. This dependence of the shape of the profile on the cluster mass is a consequence of the scale dependence introduced by cooling. According to the results shown in the previous section the rescaled central temperatures are expected to be higher for cool clusters than for hot clusters. As a consequence, the slopes of the temperature profile at the cluster center will also be higher. This dependency of the slopes on the cluster mass is more clearly illustrated in Fig. 9 and is observationally confirmed by Fig. 16 of Vikhlinin et al. (2006). In this paper the authors analyze the gas and mass-density profiles of a sample of 13 low-redshift regular clusters. For this sample spectral temperature profiles were extracted in Vikhlinin et al. (2005), and in the lower panels of Fig. 6 their best-fit profile is compared against the profiles from the cooling runs (see later). Fig. 16 of Vikhlinin et al. (2006) shows that the observed profiles for cool clusters are significantly different and steeper than for massive clusters, thus confirming the scale dependency found here in the scaled profiles.

The average profile of hot clusters is the one which is closest to the strip which is defined by the best-fit profile of Allen, Schimdt & Fabian (2001a). The agree-

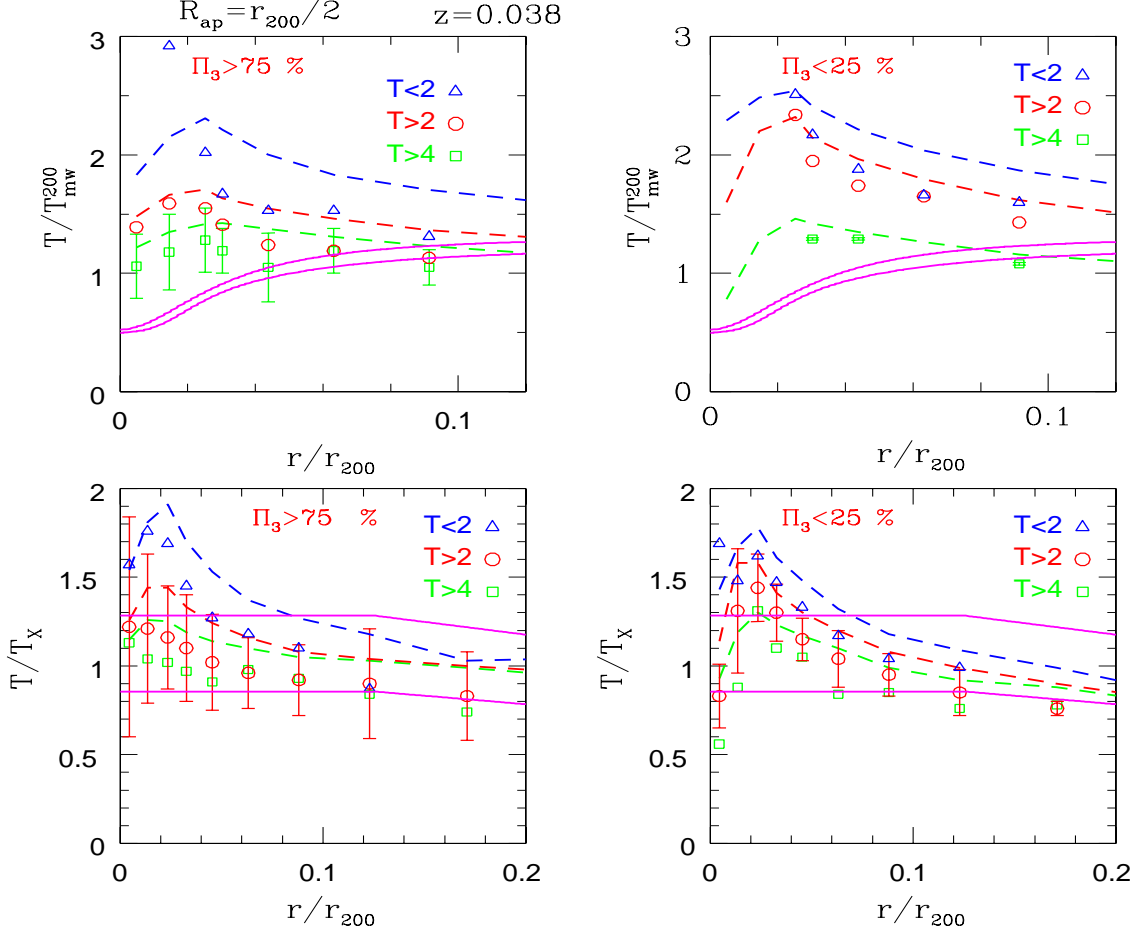


Fig. 6. Spectroscopic projected temperature profiles (points) are compared against emission-weighted profiles (dashed lines) and best-fit data constraints (solid lines). The dashed lines follow from bottom to top the same subsample order of the spectral points. The profiles are the averages over individual profiles of those clusters which are part of a subsample. These have been defined as follows : the notation $T > 4$ means that all the clusters with $T_{mw}^{200} > 4keV$ are part of the subsample, while $\Pi_3 > 75\%$ means that these clusters have a value of Π_3 above the threshold which defines the 75% of the cumulative distribution. The meaning of the other notations is similar. The power ratios have been calculated with $R_{ap} = r_{200}/2$. The upper panels have profiles extracted from the spectral sample of clusters at redshift $z = 0.038$. The profiles of the lower panels have been averaged over samples at redshifts $z = 0.116, 0.052, 0.039$ and $z = 0.025$. The solid lines of the upper panels define the 68% c.l. of the rescaled best-fit profile $T(r)/T_{mw}^{2500}$ of Allen et al. (2001a). For the lower panels the solid lines give the 68% uncertainties of the best-fit profile to the data of Fig. 18 Vikhlinin et al. (2005); temperatures are in units of T_X , the cluster emission-weighted temperature in the energy band $[0.5 - 10]keV$.

ment is significantly improved if one considers the profiles of active clusters in the left panel. In fact, the average profile of the subsample defined by both hot and active clusters is in good agreement with data, with the expectation

of the two innermost bins. These results suggest that a proper comparison of simulated profiles with the best-fit profile of Allen et al. (2001a) must take into account the mass and the morphological composition of the data sample. From Table 3 (Λ CDM) of Allen et al. there are only two clusters with $T_{2500} \simeq 6\text{keV}$, whereas $T_{mw}^{2500} \gtrsim 10\text{keV}$ for the remaining four clusters. Here the subsample of hot and active clusters has 5 members with T_{mw}^{2500} between 5 and 6keV . This implies that the scale dependency of the average profiles because of cooling is an important factor to be considered. Therefore in order to perform a careful comparison of the simulated profiles with the data of Allen et al. a sample of clusters extracted from a simulation volume much larger than the ones used here ($\simeq 1200Mpc$) is needed.

Another issue concerns the role of merging events that act on the shaping of the cluster temperature profile. The best accord with data is obtained for hot clusters which are also active, however the sample of Allen et al. consists of six clusters for which lensing mass measurements are in agreement with X-ray masses. A result which is indicative of relaxed configurations. It is worth noticing, however, that some sort of merging activity must have been at work, for at least some clusters of the sample. This is indicated by the shape of best-fit profile, which is flat or decreases towards smaller radii. This is at variance with the scaled profiles as measured from other samples (Vikhlinin et al. 2005, Piffaretti et al. 2005), which have a peak at $\simeq 0.1r_{200}$ and a decline outward. A flat profile is however what is found when moving from quiescent to active clusters: because of the mixing effects associated with the mergers the profiles have their peak height reduced or erased completely in the case of hot clusters. This behavior agrees with the findings of De Grandi & Molendi (2002), who have investigated the temperature profiles for two samples of 11 non-cooling flow clusters (NCF) and 10 cooling flow clusters (CF). For NCF clusters the authors derive profiles with a core which is approximately isothermal, which in the standard scenario is interpreted as a consequence of mergers.

In the lower panels of Fig. 6 the simulated profiles scaled in units of T_X are shown. The meaning of the symbols is the same as in the upper panels, the profiles have been obtained by averaging over cluster samples at redshifts $z = 0.116, 0.052, 0.039$ and $z = 0.025$. The solid lines indicate the scatter ($\simeq 20\%$) in the best-fit profile to the data of Fig. 18 of Vikhlinin et al. (2005), which is a sample of 13 low-redshift regular clusters. Spectral fits have been performed by Vikhlinin et al. in the energy band $[0.6 - 10]\text{keV}$, whereas the fits here are in the energy band $[0.5 - 7]\text{keV}$. The differences in the spectral fits can be considered negligible, since all the simulated clusters have $T_{mw}^{200} \lesssim 6\text{keV}$. The radial dependence of the best-fit profile is given by Eq. 2 of Vikhlinin et

al. (2005):

$$T/T_X = \begin{cases} 1.07 & \text{if } 0.035 < r/r_X < 0.125 \\ 1.22 - 1.2r/r_X & \text{if } 0.125 < r/r_X < 0.6 \end{cases}, \quad (18)$$

where $r_X = 1.95h^{-1}(T_X/10keV)^{1/2}$. The solid lines have been extrapolated in the plots downward of $r/r_{200} < 0.035$ for the sake of a comparison with the spectral points. For $r/r_{200} > 0.1$ the profiles are marginally consistent with data, at $r/r_{200} \simeq 0.2$ the simulated profiles are about $\simeq 10\% - 20\%$ lower than the central value of the best-fit profile ($T/T_X \simeq 0.1$). There is a formal improvement at $r/r_{200} < 0.1$, where the flatness of the solid lines accounts in cool cores for the scatter of the measured profiles. Clearly, a larger sample of measured profiles of cooling flow clusters is needed before it would be possible to draw statistical meaningful conclusions about the consistency of the profiles of simulated cooling clusters with data. From Fig. 15 of Vikhlinin et al. (2005), but see also Fig. 2 of Piffaretti et al. (2005), there is a clear concordance that the measured scaled profiles reach their peak values at $r/r_{200} \simeq 0.1$, whereas the simulated profiles have their peak much closer to the cluster center, at approximately $r/r_{200} \simeq 0.02$. The disagreement with data can be improved by taking advantage of the scale dependencies previously discussed and by constructing a cluster subsample of a given mass and morphological composition. However, the general framework predicts a strong correspondence between the presence of a cooling flow and a regular cluster morphology (Bauer et al. 2005, but for an alternative view see Motl et al. (2004))

Because the sample of Vikhlinin et al. consists of 11 relaxed clusters this indicates that one should compare with data the simulated profiles of the bottom right panel, rather than the profiles of active clusters of the left panel, though a proper comparison is not possible without a quantitative morphological measure of the data clusters. Although appears unlikely that the simulated temperature profiles of simulated cooling clusters can consistently fit the profiles of cooling flow clusters, note that a temperature drop at the cluster center is however qualitatively reproduced.

In Fig. 7 the sums $\sum_i \Delta T_i^2$ are shown as a function of the cluster power ratios, each panel is for a different value of the aperture radius R_{ap} . For a given cluster the sum $\sum_i \Delta T_i^2$ is defined as the sum over the radial bins, out to $r/r_{200} = 0.1$, of $\Delta T_i^2 = [(T_S(r_i) - T_{ew}(r_i))/T_{mw}^{200}]^2$. The sample investigated is the $T > 2$ in the upper panels of Fig. 6. In each panel the Spearman significance levels of the correlations are given. The main result is that there is a significant correlation between $\sum_i \Delta T_i^2$ and Π_3 , a result which indicates that the role of merging events in reshaping the temperature profiles can not be considered marginal. Moreover, for quiescent clusters the correlation between $\sum_i \Delta T_i^2$ and the cluster dynamical state appears more robust.

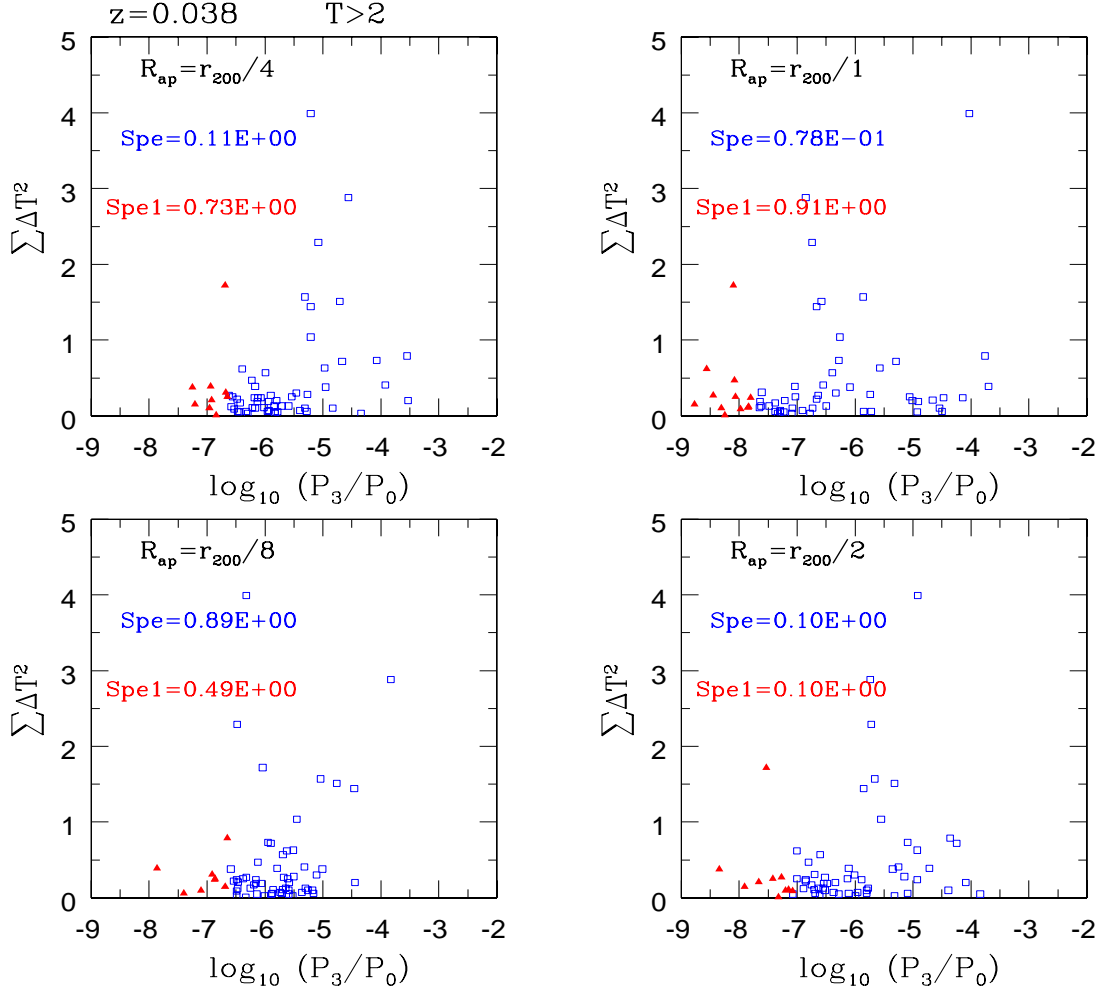


Fig. 7. The sums $\sum \Delta T^2$ versus the cluster values Π_3 . For a cluster $\sum \Delta T^2$ is defined as the sum over the radial bins, out to $r/r_{200} = 0.1$, of the squared difference $\Delta T^2 = [(T_S(r) - T_{ew}(r))/T_{mw}^{200}]^2$. The clusters are those of the sample $T > 2$ of the upper panels of Fig. 6. Each panel is for different values of R_{ap} with which the power ratios are calculated. Open squares (filled triangles) refer to all (25% percentile) of the power ratio distribution. The notation Spe= (Spe1=) gives the Spearman significance levels of the correlations.

In order to assess the consistency of the simulated profiles with previous results, for comparative purposes the work by Loken et al. (2002) was chosen, who used an adaptative Eulerian mesh hydrodynamic code. The projected emission-weighted profiles at $z = 0.038$ are shown in Fig. 8; the radial coordinate is now scaled to r_X and the horizontal scale it extends out to $r/r_X = 0.4$. The right panel is for the subsample with Π_3 below the 25% percentile, left panel is for all of the clusters. The solid line indicates the best-fit profile of

Loken et al. (2002),

$$T/T_X = T_0(1 + r/a)^{-\delta}, \quad (19)$$

where $T_0 = 1.33$, $a = r_{vir}/1.5$ and $\delta = 1.6$. Their emission-weighted profiles were constructed assuming a constant metallicity and using a $[1.5 - 11]keV$ bandpass, thus it is appropriate to compare the profile of equation (19) with simulated profiles of hot or normal ($T > 2$) clusters. The profiles of Fig. 8 are in good agreement with the best-fit profile (19) over the radial range $0.1 \leq r/r_X \leq 0.4$, with $r/r_X = 0.04$ being the lower limit to the fit. The profiles of the whole cluster sample are shallower than those of quiescent clusters and in better agreement with the profile of Loken et al. (2002). A result which indicates that the total sample is more representative of the sample of Loken et al. over which the fit was performed.

A comparison of the simulated spectral temperature profiles presented here with the data of Piffaretti et al. (2005) is not directly possible because the authors have measured their profiles using the cameras on board *XMM-Newton*. Nonetheless an indirect comparison is still possible through their Fig. 6. In this figure the authors report, together with their data points, the best-fit of equation (19). The results indicate a substantial agreement of the simulated profiles with data out to $r/r_X \simeq 0.4$. At small radii ($r \leq 0.05r_X$) a comparison of the simulated profiles with that of Loken et al. (2002) is not possible due to the radial range of the fit, though it would have been interesting because of the different numerical methods employed in the simulations. If one considers previous discussions and the profiles of Fig. 6 and 8 over their entire radial range, it turns out that the temperature profiles of cooling clusters is scale dependent and can not be considered universal, the profile of hot clusters being shallower than that of cool clusters. This is clearly illustrated in Fig. 9 (lower panels), where the dimensionless gradients $\widehat{\nabla T} \equiv d(T/T_X)/d(r/r_X)$ are evaluated at $r = 0.05r_X$ for the sample of Fig. 8 and the cluster values are shown against T_{mw}^{200} . The correlation of $\widehat{\nabla T}$ against T_{mw}^{200} is well defined, the significance levels of the linear correlations are found to be above 95%. This scale dependency has been found here clearly because of the large size of the numerical sample used; this has allowed us to subdivide the sample into subsamples according to several cluster properties, while keeping the subsamples with a statistically significant number of members.

Finally, in the top panels of Fig. 9 the dependencies of the mass accretion rates \dot{M} and the central cooling times τ_c versus the cluster dynamical state as indicated by Π_3 are investigated. Note that here the power ratios have been evaluated at $R_{ap} = r_{200}$, while $R_{ap} = r_{200}/8$ for the power ratios of the lower panels. For a given radial bin the mass accretion rate is defined as the spherical average of $\dot{M}(r) = 4\pi\rho_g r^2 v_r$, where v_r is the radial velocity of the gas. Both \dot{M} and τ_c are evaluated at a fixed radius of $50kpc$. According to

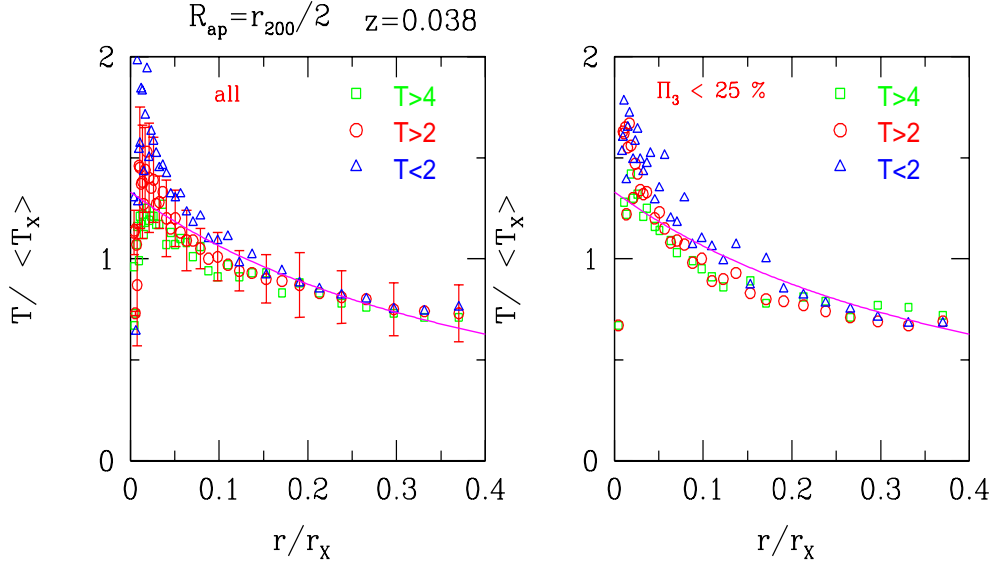


Fig. 8. Average emission-weighted profiles are displayed for different subsamples of the simulated clusters at $z = 0.038$. The notation $T > 2$ indicates, as in Fig. 6, that all the clusters with $T_{mw}^{200} > 2\text{keV}$ are part of the subsample, while $\Pi_3 < 25\%$ means that these clusters have a value of Π_3 below the threshold which defines the 25% of the cumulative distribution. T_X is the emission-weighted cluster temperature in the $[0.5 - 10]\text{keV}$ energy band and $r_X = 1.95h^{-1}(T_X/10\text{keV})^{1/2}\text{Mpc}$. Continuous line is the best-fit profile of Loken et al. (2002). Left panel is for all of the clusters while the right panel is for the cluster subsample $\Pi_3 < 25\%$, the power ratios have been calculated setting $R_{ap} = r_{200}/2$.

the standard scenario (Fabian 1994) cool gas at the cluster center will form a cooling flow as the cooling time of the gas will be shorter than the Hubble age. Spectroscopically the mass deposition rates of cooling flow clusters are found to lie in the range $\sim 10 - 500M_{\odot}\text{yr}^{-1}$. In order to maintain a steady state flow the inner region of the cluster must remain undisturbed by merging events. Therefore one expects to see some degree of correlation existing between the central cooling time τ_c , or the mass deposition rate \dot{M} , versus a morphological measure as Π_3 . From the top left panel of Fig. 9 it can be seen that the accretion rates \dot{M} have a widely scattered range of values, without displaying any clear dependence on Π_3 . The cause of the scatter is possibly due to the adopted definition of \dot{M} , which requires an estimate of the infall velocity which is subject to noise because of the local gas motion.

The cooling times τ_c show instead a significant correlation with the values of Π_3 and thus with the cluster morphology. The Spearman significance level of the correlation is $p_S = 0.03$. For quiescent clusters of the sample the average of the cooling times gives $\langle \tau_c \rangle_q = 3.75\text{Gyr}$ and for active clusters $\langle \tau_c \rangle_a = 43\text{Gyr}$. A Student t-test applied to the two distributions yields $p_t = 0.08$, so that the significance level for different means is above 90%. This is an important result

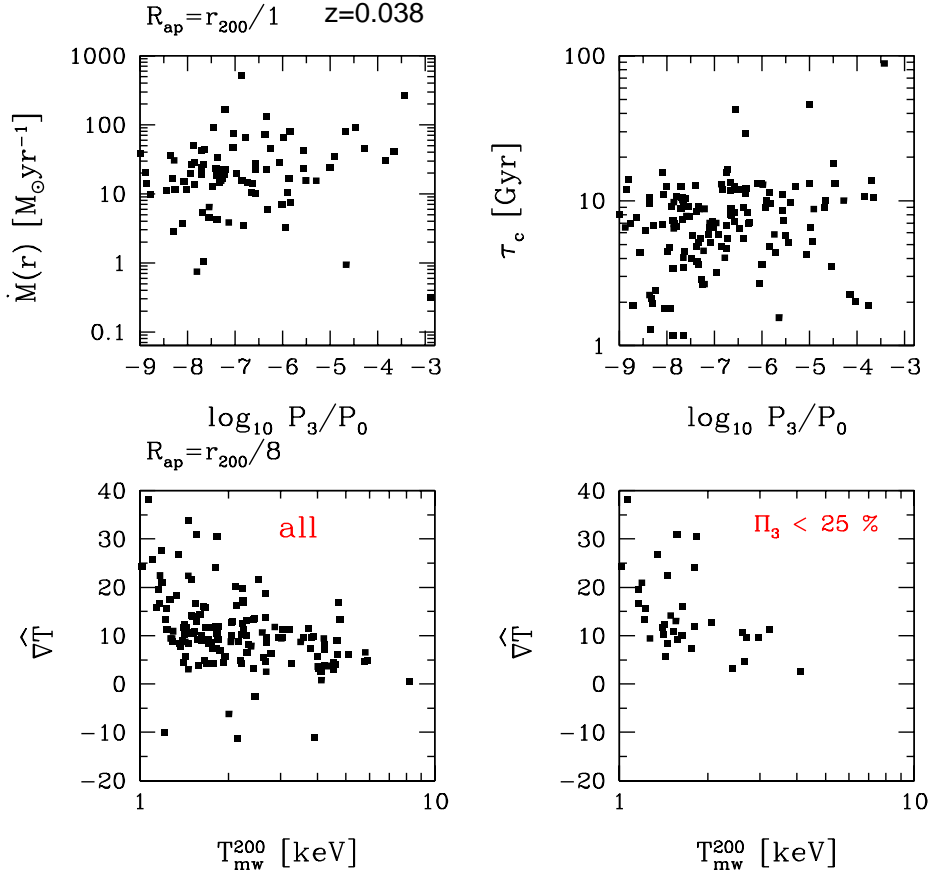


Fig. 9. The mass accretion rates and central cooling times of the simulated clusters are displayed at $z = 0.038$ in the upper panels against the power ratios $\log_{10} P_3/P_0$, these have been evaluated at $R_{ap} = \widehat{r_{200}}$. In the lower panels values at $r = 0.05r_X$ of the rescaled temperature gradient $\langle \nabla T \rangle \equiv d(T/T_X)/d(r/r_X)$ of Fig. 8 are plotted versus T_{mw}^{200} . Left (right) panel is for all (25% percentile) of the power ratio distribution, with $R_{ap} = r_{200}/8$ for the power ratios. The Spearman significance levels of the linear correlation coefficients is below 95% only for the top left panel.

because it confirms through numerical simulations the association between cluster morphologies and the strength of cooling cores. The plot can be compared with Fig. 8 of Bauer et al. (2005), who have measured from *Chandra* temperature maps the cooling times and the power ratios of 38 X-ray luminous clusters. The correlation of cooling times with Π_3 is qualitatively reproduced, though with several differences. The range of values of the simulated power ratios is higher than for data, the latter being $\lesssim 10^{-6}$. Moreover, the distribution of the central cooling times is wider for data than for the simulations, with $\tau_c \gtrsim 10Gyr$ for $\Pi_3 \gtrsim 10^{-7}$. The main source of these differences are the different aperture radii used by Bauer et al. ($R_{ap} = 0.5(h/0.7)^{-1}Mpc$) and the definition of central cooling time which is measured at the cluster innermost radial bin, and is distance dependent, whereas here a fixed radius of $50kpc$ was used.

A systematic analysis of the evolution of cool cores in galaxy clusters and how they are correlated with the cluster merger histories will be investigated in a future paper; here the results on the cooling times are used to confirm that the temperature profiles of quiescent clusters in Figures 6 and 8 can be identified with those predicted by the simulations for cooling flow clusters.

6 Numerical issues

In this section it is investigated the dependence of the results presented in this paper on the numerical resolution of the simulations. The latter is mainly controlled by two numerical input parameters: the number of simulation particles and the chosen values for the gravitational softening parameters. The most important numerical effect which must be kept under control in numerical simulations is the 2-body heating time $\tau_r(r)$, which must be at least of the order of the age of the structure and is defined as (Binney & Tremaine 1987)

$$\tau_r \simeq 6.7 \cdot 10^5 \text{Gyr} \left(\frac{\sigma_1}{10^3 \text{Kmsec}^{-1}} \right)^3 \frac{h^{-2}}{(m_d/10^{11} M_\odot)} \frac{1}{(\rho_d/\rho_c) \ln \Lambda} , \quad (20)$$

where σ_1 is the 1-D dark matter velocity dispersion, G is the gravitational constant, ρ_d is the dark matter density; $\ln \Lambda$ is the Coulomb logarithm associated to the gravitational interaction, and typical values are $\ln \Lambda \simeq 3$; The relaxation time τ_r can be estimated as follows: for a Navarro, Frenk & White (1995) dark matter density profile (Łokas & Mamon 2001) at $z = 0$ the 1-D central velocity dispersion scales as $\sigma \simeq 950 \text{km sec}^{-1} (M_{vir}/10^{15} h^{-1} M_\odot)^{1/3}$. Moreover, with the simulation method described in sect. 2, the dark particle mass m_d of the simulated cluster can be expressed as a function of the mass of the cube of size L_c and thus it scales linearly with M_{vir} . For a lattice with $N_L = 51^3$ grid points it is then easy to find that $m_d \simeq 2 \cdot 10^{-5} M_{vir}$. Accordingly, eq. 20 yields:

$$\tau_r \simeq 40 \text{Gyr} \frac{1}{(\rho_d/\rho_c)/10^5 \ln \Lambda} . \quad (21)$$

The heating time is then only weakly dependent on the cluster mass M_{vir} through the dark matter density $\rho_d(r)$. For a given cluster the heating time decreases as the density gets higher, τ_r is evaluated at the core radius $r_c \simeq 0.01 r_{200}$, approximately the resolution limit of our simulations. For the most massive cluster of the numerical sample $r_{200} \simeq 2 \text{Mpc}$, $\varepsilon_g = 25 \text{kpc}$, $\ln \Lambda \sim 2.6$ and $\rho_d/\rho_c \simeq 10^5$ at the radius r_c . The 2-body heating time is then $\tau_r \simeq 15 \text{Gyr}$. Similar values are obtained for the least massive clusters of the sample.

Table 3

Reference values for the four clusters used in the numerical tests. M_{200} : cluster mass at $z = 0$ within r_{200} in $h^{-1}M_{\odot}$, r_{200} in units of Mpc and T_{mw}^{200} in keV. The power ratio Π_3 is evaluated at $R_{ap} = r_{200}$. ε_g : value of the gas softening parameter in kpc, N_g : number of gas particles. These values are for the high resolution runs. The last two columns give the values of the stellar mass fraction $f_{star}(< r) = M_{star}(< r)/M_{tot}(< r)$ evaluated at $r = 0.1r_{200}$ and in units of Ω_b/Ω_m , for both the standard (S) and the high high-resolution (H) runs.

cluster	M_{200}	r_{200}	T_{mw}^{200}	Π_3	ε_g	N_g	$f_s(S)$	$f_s(H)$
003	$6.9 \cdot 10^{14}$	2.06	5.26	-6.45	17	212014	0.108	0.108
008	$6.2 \cdot 10^{14}$	1.99	4.6	-7.32	17	212051	0.104	0.123
092	$7 \cdot 10^{13}$	0.96	1.29	-7.17	10	211989	0.133	0.127
144	$3.3 \cdot 10^{13}$	0.75	0.95	-7.15	10	211936	0.159	0.168

This shows that, outside of the core radius, the simulations can be considered free of 2-body heating.

Another timescale which is relevant for these simulations is the cooling time $\tau_c = 3nk_B T/2\Lambda_c$, where k_B is the Boltzmann constant and n is the gas number density. According to Steinmetz & White (1997) gas cooling will be affected by artificial 2-body heating unless the dark particle mass is smaller than the critical value

$$M_c = 2 \cdot 10^9 T_6 f_{0.05} M_{\odot}, \quad (22)$$

where T_6 is the the gas temperature in units of $10^6 \text{ } ^\circ K$, $f_{0.05}$ is the ratio $f = \rho_g/\rho_d$ in units of 0.05. For the simulated clusters studied here T_6 lies in the range $T_6 \simeq 10 - 80$ and $f_{0.05} \sim 2$ for $r \lesssim 0.1r_{200}$. Thus the critical mass M_c is between $\sim 3 \cdot 10^{11} M_{\odot}$ and $\sim 4 \cdot 10^{10} M_{\odot}$. This range of values is always above the value of m_d of the corresponding cluster by a factor ~ 10 , so that the gas behavior can be considered free from numerical effects.

In order to support these conclusions, the stability of the final results against the numerical resolution of the simulations was tested by running again four different cluster simulations, but with a number of particles increased by a factor ~ 3 . The clusters were chosen in two pairs, with the constraint of being the clusters of the first pair among the most massive of the sample and those of the second pair among the least massive. The choice of the clusters was further dictated by the requirement of being in a relaxed state, therefore only those clusters with a value of the power ratio Π_3 , evaluated at $z = 0$ and at the aperture radius $R_{ap} = r_{200}$, below the threshold value which defines the 50% of the cumulative distribution were eligible. The four clusters identified according to these criteria are listed in Table 3, they are identified by their index in the sample and have $N_g \sim 210,000$. The gravitational softening parameter

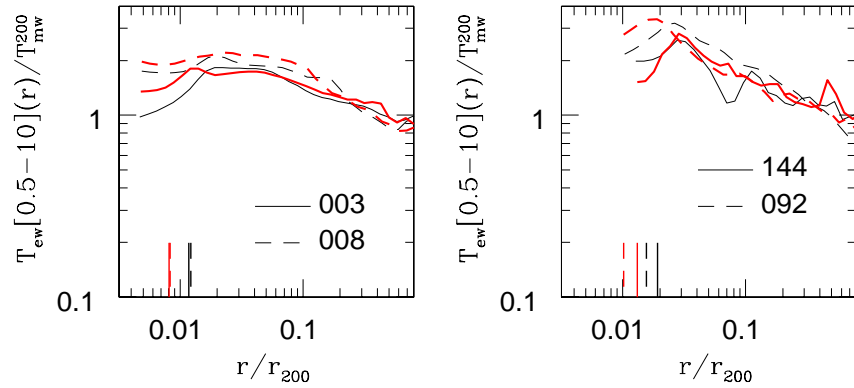


Fig. 10. Radial dependence at $z = 0$ of the temperature profiles of the four test clusters (see Table 3). Each cluster is labeled by its sample index, the standard simulations (sect. 2) are indicated by thin lines and the high resolution runs by thick (red) lines. Left panels are for the two most massive clusters and right panels for the two least massive. In the two panels are displayed the projected emission weighted temperature profiles in the $[0.5 - 10]keV$ band in units of T_{mw}^{200} , the vertical lines indicate the value of ε_g for the simulation.

for the gas particles is set to $17(10)kpc$ for the most (least) massive pair of clusters. The other numerical parameters have their values scaled accordingly. The stability of the final temperature profiles against the numerical resolution of the simulation can be estimated from Fig. 10, in which the projected emission weighted temperature profiles in the $[0.5 - 10]keV$ band are displayed in the top panels for the standard resolution and the high resolution runs. For all of the test clusters there is a good agreement between the profiles with different resolutions, indicating that convergence of hydrodynamical variables is achieved for $N_g \gtrsim 70,000$. For the less luminous clusters the similarity of the temperature profiles between runs with different resolutions shows that the peak location of the profiles is adequately resolved in the standard resolution runs and is not adversely affected by the value of ε_g .

Another numerical issue is the effect of numerical resolution on the final amount of cooled gas turned into stars. In the last two columns of Table 3 for each cluster the values of the star mass fraction $f_{star}(< r) = M_{star}(< r)/M_{tot}(< r)$, evaluated at $r = 0.1r_{200}$, are given in correspondence of the standard and high-resolution runs, respectively. The similarity of the values of f_{star} between runs with different resolution suggests that convergence is being achieved for f_{star} and that the SN feedback model implemented here effectively regulates the amount of cooled gas. These conclusions agree with previous findings of V03 (sect. 4.4), in which it was shown the stability of f_{star} against the numerical resolution of the hydrodynamic cluster simulations performed there. Finally it is worth noting that cluster X-ray properties are largely determined by the high-temperature part of the gas distribution, and

are not very sensitive to the amount of cooled gas in the cluster inner regions (V03).

7 Conclusions

In this paper results from a large set of hydrodynamic/N-body simulations of cooling clusters have been used to investigate the relationships between spectral temperatures and mass-weighted or emission-weighted temperatures. X-ray spectral temperatures have been constructed according to a set of procedures in order to reproduce spectroscopic measurements as expected from *Chandra* satellite. Spectral fits have been performed using the single-temperature *mekal* model of XSPEC, with three free parameters: the gas temperature, the metallicity abundance and the normalization. The main difference with respect to previous works which have investigated these issues is in the physical modeling of the gas, which is allowed to cool radiatively and is subject to feedback heating by SNe. This in turn implies a scale dependency of cluster X-ray properties because of the cooling efficiency to convert cold gas into stars, which is higher for cool clusters. For instance, the relationships between the global spectral temperatures T_S^Δ and the mass-weighted temperatures T_{mw}^Δ are found to be significantly biased with respect to those obtained from previous runs (ME), in which the modeling of the gas was adiabatic. The scale dependency introduced by cooling has a significant impact also on the value of T_{mw}^Δ as different cluster overdensities are considered, therefore the $T_S^\Delta - T_{mw}^\Delta$ relation is found to be strongly affected also by the value of Δ . Moreover, the scale dependency due to cooling also enters indirectly in the determination of the shape of the $T_S^\Delta - T_{mw}^\Delta$ relation because of selection effects which limit the sample construction and are dependent on the cluster mass. The biasing of spectral temperatures with respect to emission-weighted temperatures is found to be similar to that with mass-weighted temperatures, but with a wider scatter.

Another effect which governs the degree of biasing between spectral and mass-weighted temperatures is given by merging processes. Spectral temperatures, as obtained by fitting single-temperature models, can be significantly biased toward lower values than mass-weighted temperatures because of accretion of subclumps due to hierarchical clustering which contain cooler gas that modifies the photon spectrum. This source of biasing was discussed in detail by ME, here it has been analyzed using the power ratios as indicators of the cluster substructure. The main advantage of the method is the possibility to quantify the degree of substructure on a chosen scale, identified by the aperture radius R_{ap} . This scale dependency has been investigated by evaluating for the considered samples the cluster power ratio Π_3 at the aperture radius $R_{ap} \simeq R_\Delta$, in correspondence to T_S^Δ/T_{mw}^Δ for the cluster under consideration.

The results confirm the existence of a strong correlation between the ratio T_S^Δ/T_{mw}^Δ and the cluster substructure as measured by Π_3 . This correlation is found with a high significance level for all of the considered overdensities. An important result which follows from this analysis is that the biasing associated with merging events is independent from the one which follows because of the scale dependency due to cooling. Thus, the biasing of spectral temperatures in galaxy clusters is governed by two processes, independent of each other, the first being due to subclump accretion of cool gas and the second because of cooling.

This two parameter model can explain also the shape of the simulated temperature profiles. The temperature profile is however not universal even for relaxed clusters. This follows because, owing to the scale dependency introduced by cooling, the central temperature in relative units is higher for cool clusters than for hot clusters. This in turn implies for the former steeper profiles at the cluster center than for massive clusters. The gradients of the rescaled profiles are found to be dependent on T_{mw}^Δ with a high statistical significance. This scale dependency of the shape of the profiles on the cluster mass is softened or erased entirely if the cluster has undergone a number of major merger events. The profiles of these clusters are much shallower than those of quiescent clusters. This is clearly due to the effects of remixing of the gas due to mergers and these differences have been quantified according to the cluster morphology using the power ratios. It has been found that the profiles are modified in a significant way only in the presence of major mergers, where the mass of the accreting subclump is a large fraction of the cluster mass. These results were already suggested by Allen et al. (2001b, cf. sect. 9.2), but here they are confirmed through numerical simulations.

For quiescent clusters the scaled temperature profiles are in good agreement with the considered data in the radial range $0.1 \lesssim r/r_X \lesssim 0.4$. The profiles are not consistent with those measured from a sample of massive clusters (Allen et al. 2001a), but the disagreement can be made less severe if the simulated sample is constructed by taking into account the scale dependencies due to cooling and merging events. A more severe discrepancy is instead found at small radii ($r/r_X \lesssim 0.1$) between the measured profiles and those of the simulations. The profiles of the simulations reach their peak values at the scaled radial coordinate $r/r_X \simeq 0.02$, which is smaller by a factor ~ 5 of the peak location as derived by observations. Moreover, the peak height of the simulated temperature profiles is $\sim 20\%$ higher than that measured. These discrepancies are clearly indicative that the cooling model fails to consistently reproduce the observed temperature profiles. In a recent paper Motl et al. (2004) argue that hierarchical merging can provide a viable scenario for the formation and evolution of cool cores in galaxy clusters. The results of Fig. 6 indicate that merging events play a key role in reshaping the cluster profiles and support the proposed model. However, it is worth noticing that a

significant reshaping of the temperature peak is achieved only in the regime of strong merging ($\Pi_3 \gtrsim 75\%$); moreover this regime has the side effect that the central temperature drop is no longer reproduced.

The measured temperature profiles have a peak location in rescaled radial units which is located at a larger distance from the cluster center than in the simulations. This is indicative that real clusters, at some stage of their evolution, have undergone a significant diminution of their cooling rates in their cores. This is in order to provide pressure support and to prevent the inflow of gas at a higher entropy toward the cluster center. The suppression of the cooling rate is most easily achieved if the gas is heated by some energy source. The most plausible candidates are SNe whose feedback energy from their explosions can heat the gas to the desired level. However the results of the simulations performed here show that this result is not achieved even in the case of maximum theoretical efficiency of transfer of energy to the ICM. This indicates that the complex nature of the thermal structure of the cluster gas is not adequately described by the physical processes incorporated in the cooling runs performed here and suggests that additional physics is clearly needed in order to prevent overcooling in cluster cores. These results agree with previous findings and have prompted many authors to consider possible physical sources of additional heating to the ICM. The most popular models are (cf. Voit 2005 and references cited therein) energy feedback from active galactic nuclei (AGN) and thermal conduction. Because of the existing temperature gradients the latter model could in principle provide the necessary heating in the cluster central regions (Zakamska & Narayan 2003, Voigt & Fabian 2004), but is currently disfavored by more sophisticated numerical simulations which include thermal conduction (Dolag et al. 2004, Pope et al. 2005).

The most favored scenario is thus the AGN model, in which a supermassive black hole at the center of the cluster is fueled by the gas of the cooling flow and can balance the energy losses of the gas through some energy transfer. A popular mechanism involves heating of the gas due to energy dissipation of buoyant bubbles, inflated by the AGN near the cluster center and rising through the ICM (Churazov et al. 2001, Brüggen & Kaiser 2002, Fabian et al. 2002, Ruszkowski & Begelman 2002). The dissipation can occur through a number of processes, such as viscous dissipation or turbulence. It is clear that incorporating these physical processes into numerical simulations of cluster formation is a necessary step in order to explain the shape of the observed profiles. This is a very demanding computational challenge which has only recently begun to be addressed (Brüggen & Kaiser 2002, Brüggen et al. 2002, Basson & Alexander 2003, Omma et al. 2004, Ruszkowski, Brüggen & Begelman 2004, Brüggen, Ruszkowski & Hallman 2005, Sijacki & Springel 2006). In such a scenario it is difficult to assess how the main findings presented in this paper will be modified. Although a proper analysis can only be performed

through numerical simulations, several qualitative arguments can nonetheless still be used to address the effect of the interaction of the AGN with the ICM on the biasing of spectral temperatures.

In the proposed AGN heating model buoyant bubbles of plasma will rise from the cluster center toward the surrounding medium, where the transported energy will be transferred into the ICM and converted to heat. This will produce some degree of thermalization of the ICM, which in turn implies a reduction in the amount of cold gas and thus in the soft X-ray emission, thereby reducing the degree of biasing of spectral temperatures. In other words, for a given cluster mass scale, any additional source of feedback is expected to reduce the biasing. Another issue is if the scale dependency introduced by cooling will be preserved in the heating scenario. Some degree of modification will be present, since the bubble injection energy, E_{bub} , is scale dependent itself, according to the black hole mass. For example, in one of their models Sijacki & Springel (2006) propose $E_{bub} \propto M_{200}^{4/3}$, and therefore in relative terms the energy feedback is higher for massive clusters. The effects on the thermal status of the ICM of energy feedback from AGN are however not expected to modify in a significant way the scale dependency due to cooling. This argument is mainly supported by recent measurements of spectral temperature profiles for a sample of cooling flow clusters (Vikhlinin et al. 2005, 2006). The radial behavior of the measured profiles for cool clusters is significantly different and steeper than for massive clusters, which is in qualitative agreement with what found here. These conclusions are valid if the cluster possesses a regular X-ray morphology, which is indicative of a dynamically relaxed status. In the case of an ongoing merger large amount of cold gas could be supplied at the cluster center, thus replenishing the gas reservoir of the black hole and triggering AGN activity. In this scenario the thermal status of the ICM surrounding the black hole will be due to a complex interplay between the accretion of cold gas and the uplifted bubble energy. This suggests that the scale dependency depicted in Fig. 4 will be most likely modified in the proximity of a major merger event ($\Pi_3 \rightarrow 0$), with a decrease in the spectral bias owing to the feedback energy due to accretion and injected into the ICM. Such a complex picture can however be addressed self-consistently only through numerical simulations.

To summarize, it is worth noting, however, that any proposed heating model must be able to explain the lack of cold gas at the cluster center as well as the observed peak location of the temperature profile. Finally, the results of this paper indicate that in order to properly compare X-ray properties of simulated clusters with those observed, the mass and the morphological composition of the sample must be carefully taken into account.

Acknowledgments

The author is grateful to K. Arnaud, A. Gardini and P. Tozzi for their helpful comments and patient explanations which made it possible to develop the procedures described in sect. 3.

References

- Allen, S.W. & Fabian, A.C. 1998, MNRAS, 297, L57
- Allen, S.W., Schimdt, R.W. & Fabian, A.C. 2001, MNRAS, 328, L37
- Allen, S.W., Fabian, A.C., Johnstone, R.M., Arnaud, K.A. & Nulsen, P.E.J. 2001, MNRAS, 322, 589
- Anninos, P. & Norman, M.L. 1996, ApJ, 459, 12
- Arimoto, N. & Yoshii, Y. 1987, AA, 173, 23
- Ascasibar, Y., Yepes, G., Müller, V. & Gotllöber, S. 2003, MNRAS, 346, 731
- Basson, J.F. & Alexander, P. 2003, MNRAS, 339, 353
- Bauer, F.E., Fabian, A.C., Sanders, J.S., Allen, S.W. & Johnstone, R.M. 2005, MNRAS, 359, 1481
- Bialek, J.J., Evrard, A.E. & Mohr, J.J. 2001, ApJ, 555, 597
- Binney, J., Tremaine, S., 1987, *Galactic Dynamics*, Princeton: Princeton Univ. Press
- Borgani, S., Murante, G., Springel, V., Diaferio, A., Dolag, K., Moscardini, L., Tormen, G., Tornatore, L. & Tozzi, P. 2004, MNRAS, 348, 1078
- Böhringer, H., Matsushita K., Churazov E., Ikebe Y., & Chen, Y. 2002, AA, 382, 804
- Brüggen, M. & Kaiser, C.R. 2001, MNRAS, 325, 676
- Brüggen, M. & Kaiser, C.R. 2002, Nature, 418, 301
- Brüggen, M., Kaiser, C.R., Churazov, E. & Enßlin, T.A. 2002, MNRAS, 331, 545
- Brüggen, M., Ruszkowski, M. & Hallman, E. 2005, ApJ, 630, 740
- Bryan, G.L. 2000, ApJ, 544, L1
- Buote, D.A. & Tsai, J.C. 1995, ApJ, 452, 522
- Buote, D.A. 2002, in Feretti, L., Gioia, I.M. & Giovannini, G., eds, *Merging Processes in Cluster of Galaxies*, Kluwer, Dordrecht astro-ph/0106057

Buote, D.A., Valdarnini, R., Hart, B.C., Humprey, P.J. 2006, in preparation

Churazov, E., Brüggén, M., Kaiser, C.R., Böhringer, H. & Forman, W. 2001, ApJ, 554, 261

David, L.P., Slyz, A., Jones, C., Forman, W., Vrtilék, S.D. & Arnaud, K.A. 1993, ApJ, 412, 479

Dolag, K., Jubelgas, M., Springel, V., Borgani, S. & Rasia, E. 2004, ApJL, 606, L97

De Grandi, S. & Molendi, S. 2002, ApJ, 567, 163

Ebeling, H., Edge, A.C., Fabian, A.C., Allen, S.W., Crawford, C.S. & Böhringer, H. 1997, ApJ, 479, L1

Ebeling, H., Edge, A.C., Böhringer, H., Allen, S.W., Crawford, C.S., Fabian, A.C., Voges, W. & Huchra, J.P. 1998, MNRAS, 301, 881

Edge, A.C., Stewart, G.C., Fabian, A.C. & Arnaud, K.A. 1990, MNRAS, 245, 559

Evrard, A.E. & Henry, J.P. 1991, ApJ, 383, 95

Fabian, A.C. 1994, ARAA, 32, 277

Fabian, A.C., Celotti, A., Blundell, K.M., Kassim, N.E. & Perley R.A. 2002, MNRAS, 331, 369

Gardini, A., Rasia, E., Mazzotta, P., Tormen, G., De Grandi, S. & Moscardini, L. 2004, MNRAS, 351, 505

Henry, J.P. & Arnaud, K.A. 1991, ApJ, 372, 410

Henry, J.P., Gioia, I.M., Maccacaro, T., Morris, S.L., Stocke, J.T. & Wolter, A. 1992, ApJ, 386, 408

Henry, J.P. 1997, ApJ, 489, L1

Hernquist, L. & Katz, N. 1989, ApJS, 70, 419

Jubelgas, M., Springel, V. & Dolag, K. 2004, MNRAS, 351, 423

Kaiser, N. 1991, ApJ, 383, 104

Kaastra, J.S., Ferrigno, C., Tamura, T., et al. 2001, AA, 365, L99

Katz, N. & White, S.D.M. 1993, ApJ, 412, 455

Lewis, G.F., Babul, A., Katz, N., Quinn, T., Hernquist, L. & Weinberg, D.H. 2000, ApJ, 536, 623

Lewis, A.D., Stocke, J.T. & Buote, D.A. 2002, ApJL, 573 L13

Loewenstein, M. & Mushotzky, R. 1996, ApJ, 466, 695

Loewenstein, M. 2001, ApJ, 557, 573

Lokas, E.L. & Mamon, G.A. 2001, MNRAS, 321, 155

Loken, C., Norman, M.L., Nelson, E., Burns, J., Bryan, G.L. & Motl, P. 2002, ApJ, 579, 571

Markevitch, M. 1998, ApJ, 504, 27

Markevitch, M., Forman, W.R., Sarazin, C.L. & Vikhlinin, A. 1998, ApJ, 503, 77

Markevitch, M., et al. 2000, Apj, 541, 542

Markevitch, M. & Vikhlinin, A. 2001, Apj, 563, 95

Markevitch, M., Gonzalez, A.H., David L., Vikhlinin, A., Murray, S., Forman, W., Jones, C. & Tucker, W. 2002, ApJL, 567, L27

Mathiesen, B. & Evrard, A.E. 2001, ApJ, 546, 100 ME

Mazzotta, P., Rasia, E., Moscardini, L. & Tormen, G. 2004, MNRAS, 354, 10

Mohr, J.J., Evrard, A.E., Fabricant, D.G. & Geller, M.J. 1995, ApJ, 447, 8

Motl, P.M., Burns, J.O., Loken, C., Norman, M.L. & Bryan, G. 2004, ApJ, 606, 635

Muanwong, O., Thomas, P.A., Kay, S.T. & Pearce, F.R. 2002, MNRAS, 336, 527

[Navarro, Frenk & White (1995)] Navarro, J., Frenk C.S. & White, S.D.M. 1995, MNRAS, 275, 720

Omma, H., Binney, J., Bryan, G. & Slyz, A. 2004, MNRAS, 348, 1105

Pearce, F.R., Thomas, P.A., Couchman, H.M.P. & Edge, A.C. 2000, MNRAS 317, 1029

Peterson, J.R., Paerels, F.B.S., Kaastra J.S. et al., 2001 AA, 365, L104

Piffaretti, R., Jetzer, Ph., Kaastra, J.S. & Tamura, T. 2005, AA, 433, 101

Pope, E.C.D., Pavlovski, G., Kaiser, C.R. & Fangohr, H. 2005, MNRAS, 364, 13

Rasia, E., Mazzotta, P., Borgani, S., Moscardini, L., Dolag, K., Tormen, G., Diaferio, A., Murante, G. 2005, ApJL, 618, L1

Raymond, J.C. & Smith, B.W. 1977, ApJS, 35, 419

Reynolds, C.S., McKernan, B., Fabian, A.C., Stone, J.M. & Vernaleo, J.C. 2005, MNRAS, 357, 242

Richstone, D., Loeb, A. & Turner, E.L. 1992, ApJ, 393, 477

Rosati, P., Della Ceca, R., Norman, C. & Giacconi, R. 1998, ApJ, 492, L21

Rosati, P. et al., 2004, AJ, 127, 230

Ruszkowski, M. & Begelman, M.C. 2002, ApJ, 581, 223

Ruszkowski, M., Brüggem, M. & Begelman, M.C. 2004, ApJ, 611, 158

Sarazin, C.L. 1986, Reviews of Modern Physics, 58, 1

Sijacki, D. & Springel, V. 2006, MNRAS, 366, 397

Steinmetz, M. & White, S.D.M. 1997, MNRAS, 288, 545

Suginohara, T. & Ostriker, J.P. 1998, ApJ, 507, 16

Sutherland, R.S. & Dopita, M.A. 1993, ApJ, 88, 253

Tamura, T., Kaastra, J.S., Peterson, J.R., et al. 2001, AA, 365, L87

Tornatore, L., Borgani, S., Springel, V., Matteucci, F., Menci, N. & Murante, G. 2003, MNRAS, 342, 1025

Valageas, P. & Silk, J. 1999, ApJ, 350, 725

Valdarnini, R., Ghizzardi, S. & Bonometto, S. 1999, New Astr, 4, 71

Valdarnini, R. 2002, ApJ, 567, 741

Valdarnini, R. 2003, MNRAS, 339, 1117

Vikhlinin, A., Markevitch, M. & Murray, S.S. 2001, ApJ, 551, 160

Vikhlinin, A. 2006, ApJ, 640, 710

Vikhlinin, A., Markevitch, M., Murray, S.S., Jones, C., Forman, W. & Van Speybroeck, L. 2005, ApJ, 628, 655

Vikhlinin, A., Kravtsov, A., Forman, W., Jones, C., Markevitch, M., Murray, S.S. & Van Speybroeck, L. 2006, ApJ, 640, 691

Voit, G.M. & Bryan, G.L. 2001, Nature, 414, 425

Voigt, L.M., Schmidt, R.W., Fabian, A.C., Allen, S.W. & Johnstone, R.M. 2002, MNRAS 335, L7

Voigt, L.M. & Fabian, A.C. 2004, MNRAS, 347, 1130

Voit, G.M. 2005, RMP,77,207

White, R.E. 1991, ApJ, 367, 69

Yoshikawa, K., Jing, Y.P. & Suto, Y. 2000, ApJ, 535, 593

Zakamska, N.L. & Narayan, R. 2003, ApJ, 582, 162